Microwire Sensors based on Optical Fiber Tapers

U.PORTO

FACULDADE DE CIÊNCIAS
UNIVERSIDADE DO PORTO

Ricardo Melo André

Departamento de Física e Astronomia
Faculdade de Ciências

Universidade do Porto

A dissertation submitted for the degree of

Master in Physical Engineering

Porto 2012

Jury President and MIEF Course Director

António Manuel Pais Pereira Leite, Associate Professor, Department of Physics and Astronomy, Faculty of Sciences, University of Porto

Supervisors

Orlando José dos Reis Frazão, Senior Researcher, Institute for Systems and Computer Engineering of Porto
Manuel Joaquim Bastos Marques, Assistant Professor, Department of Physics and Astronomy, Faculty of Sciences, University of Porto

External Examiner

Rogério Nunes Nogueira, Invited Assistant Professor, Department of Physics, University of Aveiro

Date of Graduation

October 12$^{\text{th}}$, 2012

Acknowledgements

It would not have been possible to write this master's dissertation without the help and support of the people around me, to only some of whom it is possible to give particular mention here.

This dissertation would not have been possible without the help, support and patience of my principal supervisor, Dr. Orlando Frazão. His knowledge and ideas were invaluable. The good advice and support of Professor Manuel Bastos Marques has been essential on an academic and scientific level, for which I am extremely grateful.

I am most grateful to INESC Porto, more specifically the Optoelectronics Unit, and all my colleagues for welcoming me and helping me in any, and every way they could. Thanks go out to Susana Silva for her help in many aspects of lab work. A special mention to my lab partner Rita Ribeiro for listening to my rants every day without once complaining.

I would like to acknowledge the financial support provided by *Fundação Calouste Gulbenkian* through the award *Prémio de Estímulo à Investigação*. Thanks also to the european COST TD 1001 action that supported my work when I had the need to go abroad. I would like to thank the Institute for Photonic Technology (IPHT) in Jena, in particular Professor Hartmut Bartelt, Dr. Martin Becker and Tina Eschrich for their indispensable support during the time I spent at the institute. Thanks also go to the University of Campinas, São Paulo, and Professor Cristiano Cordeiro for his help in producing some of the structures used in this work.

Last, but by no means least, my parents, my family and my friends who have given me their unequivocal support for which my mere expression of gratitude does not suffice.

Abstract

This dissertation explores the study and development of fiber optic devices based on tapers. The main objective is to understand the tapers' behavior when subjected to mechanical stress. Initially, a brief synthesis of the advances in the area of fiber sensors based on this technology is performed, including aspects related to taper profiles, fabrication, and the theoretical model of taper strain distribution.

The dissertation can be divided into two scientific parts. The first part is the application of two sensors based on conventional fibers, one using a singlemode-multimode-singlemode fiber structure and the other using long period gratings. Intermodal interference is the basis of the first structure. A taper is fabricated in the multimode region in order to obtain a reduction in the number of guided modes. The second structure consists of a long period grating written in a taper. These two types of sensors are characterized in strain and temperature. The second part of the dissertation is dedicated to the study of tapers in microstructured optical fibers, specifically in suspended core fibers. Two fibers with different geometry, namely with a suspended core of three or four holes, are studied. The first fiber has a high birefringence due to its triangular geometry and the second one is multimode due to the size of its core and the index difference between core and air cladding. Initially some modal simulations are performed for each geometry. While the triangular-core fiber is studied in a fiber loop mirror configuration, the other is analyzed in transmission as an intermodal interferometer. Obtaining nanometric cores by fabricating tapers in microstructured optical fibers is achieved. Both sensors are characterized in strain and temperature.

Some suggestions of future lines of investigation about sensor technology based on tapers are presented.

Resumo

Esta dissertação apresenta o estudo e o desenvolvimento de dispositivos em fibra óptica baseados em *tapers*. O principal objectivo é compreender o comportamento dos *tapers* quando sujeitos a tensão mecânica. Inicialmente faz-se um resumo dos avanços na área de sensores baseados nesta tecnologia, incluindo aspectos relativos a perfis de *tapers*, à sua fabricação e ao modelo teórico que explica o seu comportamento sob tensão mecânica.

A dissertação pode dividir-se em duas partes científicas. A primeira parte é a utilização de sensores em fibras convencionais, nomeadamente uma utilizando a estrutura monomodo-multimodo-monomodo e a outra baseada em redes de período longo. O modo de funcionamento da primeira estrutura é baseado na interferência multimodal. Na região multimodo é fabricado um *taper* de forma a obter uma redução do número de modos guiados. A segunda estrutura consiste numa rede de período longo escrita num *taper*. Estes dois tipos de sensores são caracterizados quanto à sua sensibilidade a tensão mecânica e a temperatura. A segunda parte da dissertação é dedicada ao estudo de *tapers* em fibras microestruturadas, em especial nas fibras de núcleo suspenso. São estudadas duas fibras com geometria diferente, nomeadamente com núcleo suspenso de três e quatro alvéolos. A primeira fibra é de elevada birrefringência devido à sua geometria triangular e a segunda é multimodo devido à dimensão do seu núcleo e à diferença de índice entre núcleo e baínha de ar. Inicialmente são realizadas simulações do número de modos para cada geometria. Enquanto que a fibra de núcleo triangular é estudada numa configuração em anel formando um espelho em fibra, a outra fibra é analisada em transmissão como um interferómetro intermodal. São obtidos núcleos com dimensões nanométricas fabricando *tapers* na fibra microestruturada. Os dois tipos de sensores são caracterizados quer em tensão mecânica quer em temperatura.

Por fim, são apresentadas algumas sugestões para dar continuidade à investigação sobre a tecnologia de sensores baseados em *tapers*.

Contents

List of Figures

List of Tables

Nomenclature

B Phase Birefringence

G Group Birefringence

N Number of Guided Modes

V Normalized Frequency

BPM Beam Propagation Method

FBG Fiber Bragg Grating

FLM Fiber Loop Mirror

HiBi Highly Birefringent

LPG Long Period Grating

MMF Multimode Fiber

MMI Multimode Interference

MOF Microstructured Optical Fiber

SCF Suspended Core Fiber

SMF Single Mode Fiber

SMS Singlemode-Multimode-Singlemode

Chapter 1

Introduction

The emergence of optical fibers led to the development of many industries and scientific areas. Certainly the most important was the boom in optical communications. The increasing need to transport information at ever higher speeds expedited the development of optical fibers. Many types of fibers were developed in this context such as singlemode fibers (of which special relevance must be given to SMF 28), multimode fibers and other dispersion related fibers.

More recently, microstructured optical fibers (MOFs) have appeared and present novel properties that allow novel applications [1]. The main contribution, to date, that arose from MOFs is the generation of supercontinuum. This effect happens when a pulse interacts nonlinearly with the material and a substantial spectral broadening occurs that may lead to the generation of white light [2].

Optical communications were not the only area where optical fibers found great success. Optical fibers also brought great advantages to sensing. Optical fiber sensors are devices in which the physical, chemical or biological parameter that needs to be measured is directly linked with changes of an optical parameter of the guided light. These optical parameters can be intensity, phase, polarization or wavelength and the interaction of the measurand can be with one or more of these parameters. Optical fiber sensors present some properties that make them more attractive than conventional electrical sensors for certain applications. They have a reduced dimension, are immune to electromagnetic interference and can be operated remotely. The great advantage of optical fiber sensors is the fact that optical fibers are simultaneously the sensor and the communication channel allowing for remote sensing without the need of a local monitoring system.

Currently, the hottest research area in sensors is the development of sensing heads designed on microstructured fibers. Due to the control of their geometry during fabrication and the possibility of using techniques such as femtosecond lasers to write Fiber Bragg Gratings (FBGs) [3] or CO_2 lasers to write Long Period Gratings (LPGs) [4] it is possible to easily design new sensors. Other very interesting sensors can be tapers in optical fiber fabricated by flame-brushing [5], focused CO_2 lasers [6], electric arc [7] or filament heating [8]. An emerging area is the combination of several structures namely, tapers + LPGs [9] or tapers + interferometers [10], that can lead to an enhanced performance of the sensing heads. One such enhancement is the decrease of cross sensitivity to temperature achieved with sensors written in microstructured fibers. This is the context in which this dissertation is inserted. In this work several structures are combined with the objective of obtaining enhanced sensors.

This dissertation is divided into seven chapters. This first chapter describes the motivation for this work and the main goals that are to be achieved with it. It also includes the publications that resulted from this master's program. Chapter 2 presents an overview of optical fiber tapers. It starts with a brief historical context of optical fiber tapers, especially their applications in sensing. A brief analysis of the taper structure and its fabrication techniques is performed. Special relevance is given to the VYTRAN glass processing workstation as it is used to fabricate several tapers used in this work. Finally, a theoretical analysis of the strain sensitivity behavior of a tapered structure when it is subjected to tensile stress is performed.

Chapter 3 starts with a brief introduction to multimode interference devices giving special relevance to singlemode–multimode–singlemode (SMS) fiber structures. Tapers with different waist diameters are produced on SMS fiber structures and characterized in strain and temperature. Some simulations are presented to obtain a clearer overview of what is happening inside these structures. A simultaneous strain and temperature measurement scheme is proposed, as a proof of concept, by using two of these structures with different diameters. Finally, a stability analysis is performed on this system.

Chapter 4 is focused on long period gratings (LPGs) and on the advantage of writing such gratings on the tapered section of a fiber. Following a short introduction to LPGs and their applications in sensing, an explanation on how the tapered LPGs were produced is presented. A comparison with two more common situations, single LPG and LPG in series with a taper, is shown. Finally, a characterization of the tapered LPG structures relative to strain and as a function of total fiber length is performed.

Chapter 5 introduces microstructured optical fibers (MOFs) with special focus on suspended core fibers and their tapering. Tapers of different waist diameters on four-hole suspended core fiber are analyzed. Modal simulations and spectral responses as well as strain and temperature characterizations are discussed.

In Chapter 6, after a brief introduction to fiber loop mirrors and their applications, the operation method of a fiber loop mirror is explained. In this chapter, as with the previous one, the structures analyzed are tapers in suspended core fiber. In this case, the suspended core fiber has only three holes and is characterized inside a fiber loop mirror. Besides the usual temperature and strain characterizations, a group birefringence analysis was also performed on the group of tapers.

Finally, Chapter 7 sums up the whole thesis and compares the results obtained with the distinct structures. It also presents some guidelines to pursue in future work.

The main goal of this master's dissertation is the study of novel sensors based on tapers. Associating the tapers with other structures makes it possible to obtain new and perhaps enhanced devices. In this manner, the main objectives of this master's degree are the:

- Study of new structures based on fiber tapers;
- Study of the combination of fiber tapers with other fiber structures such as long period gratings;
- Study of suspended core fibers and their tapering process to obtain very small waveguides (suspended cores) and explore them for sensing;
- Study of several interferometric configurations using these tapered structures for enhanced sensing.

Now, the scientific publications and conference attendances that resulted from this master's thesis are presented.

Scientific Publications

R. M. André, S. O. Silva, M. Becker, K. Schuster, M. Rothardt, H. Bartelt, M. B. Marques, and O. Frazão. Strain Sensitivity Enhancement in Suspended Core Fiber Tapers. *Photonic Sensors*, 2012, DOI: 10.1007/s13320-012-0059-2.

R. M. André, C. R. Biazoli, S. O. Silva, M. B. Marques, C. M. B. Cordeiro, and O. Frazão. Simultaneous strain and temperature measurement based on multimode interference in tapered fiber structures. *Photonics Technology Letters*, 2012. (Accepted)

Conferences

R. M. André, S. O. Silva, M. Becker, K. Schuster, M. Rothardt, H. Bartelt, M. B. Marques, and O. Frazão. Strain Characterization of Suspended-Core Fiber Tapers. In *SPIE Photonics Europe*, Brussels, Belgium, April 16–19 , 2012. (Oral Presentation)

R. M. André, M. B. Marques, P. Mergo, and O. Frazão. Fiber Loop Mirror using a Suspended Micro-Core Fiber for Strain Sensing. In *X SEONS*, Porto, Portugal, June 27-29, 2012.

R. M. André, M. B. Marques, and O. Frazão. Interferómetro de Sagnac usando uma Fibra de Núcleo Suspenso. In *Física 2012 - 18ª Conferência Nacional de Física*, Aveiro, Portugal, September 6–8, 2012. (Poster Presentation)

R. M. André, S. O. Silva, M. B. Marques, C. M. B. Cordeiro, and O. Frazão. High Strain Sensitivities using Multimode Interference in Tapered Single mode-Multimode-Single mode Fiber Structures. In *22nd International Conference on Optical Fiber Sensors* (OFS-22), Beijing, China, October 14–19, 2012. (Accepted)

Chapter 2

Tapers

2.1 Historic Context

Optical fiber tapers are devices that have a wide range of applications and that have become essential in optical communications and optical sensing. Tapers were first used to fabricate single-mode fiber couplers with great success [11]. Since then, and besides couplers, they have been applied to beam expanders [12], to interferometers (such as the Mach-Zehnder in fiber) [13], and inevitably, to sensors [14-17].

The taper's first applications in sensing took advantage of its most obvious characteristic – the interaction of the evanescent field of the guided mode with the external medium, resulting in an optical refractometer [14]. From there, tapers started being used for diverse sensing applications such as curvature [15] and pressure [16].

Tapers are also combined with other structures such as Fiber Bragg Gratings (FBGs) and Long Period Gratings (LPGs) for novel sensing configurations. A sensor using a chirped Bragg grating written in the taper region for strain-temperature discrimination [17] and an optical inclinometer based on a taper combined with an LPG [9] are just two examples.

Many interferometric configurations with tapers have been studied. Some examples that use tapers in single-mode fiber are a refractive index sensor based on a Michelson interferometer [10] and a strain sensor based on an in-line Mach-Zehnder interferometer [18]. Another interesting example is an optical flowmeter based on a modal interferometer with a nonadiabatic taper [19].

All the examples given refer to tapers in single-mode standard fiber. With the development of novel microstructured optical fibers (MOFs), tapers have again regained the spotlight because new effects and enhanced sensitivities can be obtained. Only recently has the tapering of MOFs been perfected [20]. Research is now changing its focus from the tapering process itself to the application of such tapered MOFs. For example, tapered MOFs are being studied for supercontinuum generation [21], and new applications in optical sensing are being explored [22].

2.2 Taper Structure and Fabrication

Tapering optical fiber involves reducing its diameter by heating and stretching the fiber. There are a variety of heat sources that can be used to produce a taper such as a gas burner [5], a focused CO_2 laser [6], or an electric arc formed between a pair of electrodes just like in a fusion splicer [7]. The combination of the heat source with a stretching strategy allows a large number of taper profiles to be obtained. Tapers can be modeled assuming several types of profiles, namely: linear, exponential, parabolic, sinusoidal, and polynomial, among others [23]. In order to deduce the fiber shape from the tapering conditions, detailed data from the stretching, the heat source and its temperature distribution would be needed for a fluid mechanics analysis. The theoretical background was thoroughly developed in the late ’80s and early ’90s, mainly by Birks and Li [23], Love *et al.* [24, 25, 26], and Black *et al.* [27]. This type of analysis will not be performed here. In Figure 2.1 two models of taper profiles are represented. These two models were fabricated using the VYTRAN and the 3SAE as explained in section 2.2.1.

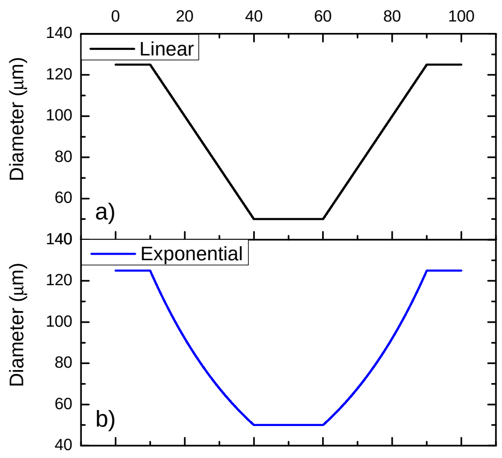

Figure 2.1 – Two models of taper profiles: a) linear and b) exponential.

A fiber taper can be seen as a three-part structure as schematically shown in Figure 2.2:

1. A conical section where the fiber diameter gradually decreases. This section is not necessarily linear, as seen in Figure 2.1.

2. A section of fiber with a uniform diameter, smaller than the initial untapered fiber's diameter, called the *taper waist*. This section can be long, short or even nonexistent.

3. A second conical section where the fiber diameter gradually increases up to the original size.

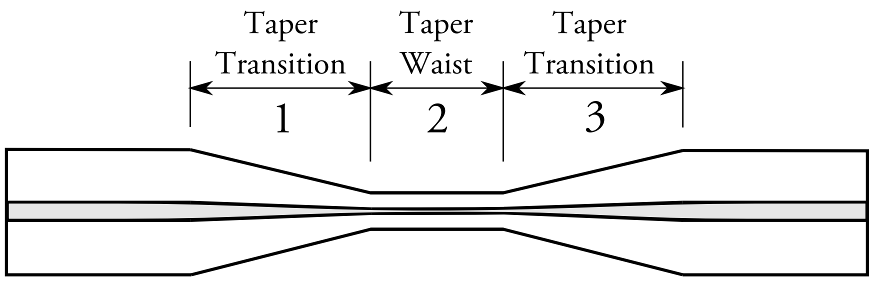

Figure 2.2 – Taper schematics: 1. *Down-taper*; 2. Taper waist; 3. *Up-taper.*

2.2.1 VYTRAN – Glass Processing Workstation

Most of the tapers used in the scope of this thesis were produced using a VYTRAN Glass Processing Workstation (GPX-3400 series). The VYTRAN is a glass processing platform that performs fusion splicing and tapering of specialty fibers. The system consists of a filament heater, precision stages with multi-axis control (fiber holding blocks), a microscopic high resolution CCD imaging system, and a personal computer. The filament heater has a wide temperature range from several hundred up to 3000 °C, which makes it possible to fuse and process various fiber types and sizes. The fiber holding blocks allow precise control and alignment of the fiber for high quality splicing and tapering. Figure 2.3 shows the setup of the GPX-3400 and a detail of the filament heater.

The working principle is based on heating a portion of fiber in the filament heater to its softening point while applying a tensile force by pulling the fiber with the holding blocks. As the fiber elongates, its cross sectional area will be reduced accordingly. Taper properties can be controlled by a graphic interface. In order to taper, the VYTRAN's fiber holding blocks do not travel in opposite directions as first expected but in the same direction at different velocities. When the VYTRAN first starts stretching the fiber and tapering it down (transition region), it creates what is referred to as the down taper. When the fiber reaches the desired taper waist diameter, the GPX stops stretching the fiber any further and maintains a constant tension on the

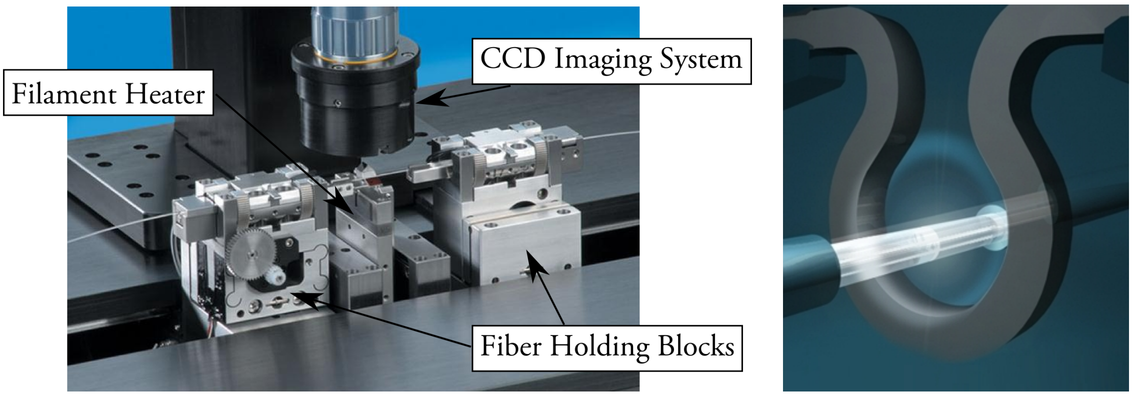

(a) Workstation photograph. **(b)** Filament heater detail.

Figure 2.3 – VYTRAN GPX-3400 - Glass processing workstation.

fiber to produce the constant diameter section – the taper waist. After the waist has been created, the GPX decreases the tension on the fiber until it finally stops stretching; it has now created the second transition region – the up taper. Other parameters such as filament power, pull velocity, and taper load positions can be controlled to adapt the taper conditions to the type of fiber and the taper dimensions desired. Due to the intrinsic properties of the VYTRAN GPX-3400 it can only produce linear transition regions in theory. Effectively, this depends on each situation in particular. In Figures 2.4a and 2.4b, taper profiles of tapers produced with the VYTRAN are shown.

Just for comparison, in Figure 2.4c, a taper produced with a different device (3SAE Large Diameter Splicing System) has completely different taper transition regions. In this case, the transition regions are exponential.

2.3 Theoretical Model of Taper Strain Distribution

When applying strain to a uniform-diameter fiber, the strain is equally distributed along its entire length. If the fiber structure does not have homogeneous diameter along its length then the strain distribution will not be uniform. The local strain will be larger at points where the fiber structure's cross-sectional area is smaller and *vice-versa*. The nonuniform strain distribution that arises, if applied correctly, may be useful for discriminating two different physical parameters such as temperature and strain when cross-sensitivity exists, or even enhancing the strain sensitivity of a

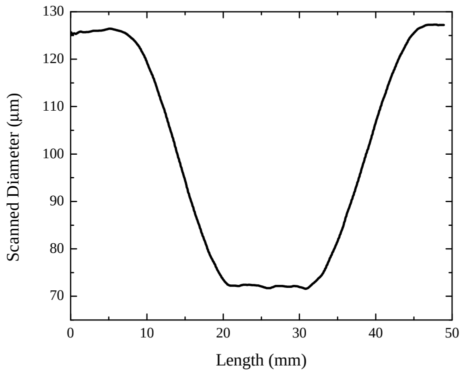

(a) 70 μm taper produced with the VYTRAN GPX-3400

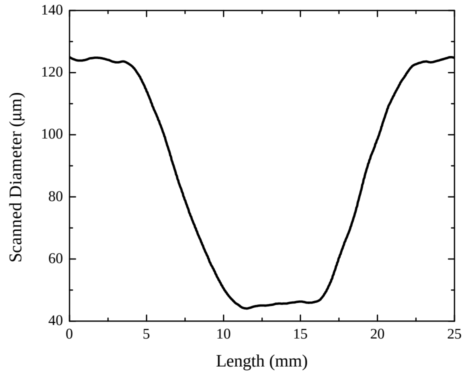

(b) 45 μm taper produced with the VYTRAN GPX-3400

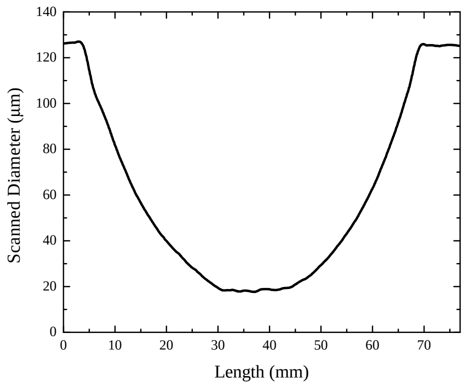

(c) 20 μm taper produced on a 125 μm fiber using the 3SAE.

Figure 2.4 – VYTRAN GPX-3400 produced tapers

fiber structure. James *et al.* used two fiber Bragg gratings (FBGs) written on both sides of a splice between two fibers of different diameter to obtain different strain responses to an applied stress and consequently measure simultaneously temperature and strain [28]. Xiaohong *et al.* etched part of an FBG to obtain different diameter sections and thus be able to discriminate between temperature and strain [29]. More recently, Frazão *et al.* bonded a dummy fiber to one of two FBGs written in series just to increase the cross-sectional area and obtain different local strains on each FBG; this allowed the discrimination of strain and temperature [30]. One final example is the use of a taper in series with an FBG to be able to tune the strain sensitivity of the Bragg wavelength by acting on the total fiber length [31].

When analyzing the strain sensitivity of tapered fiber structures, i.e., structures with different diameters along their length one needs to take into account the non-uniform strain distribution along the length of the sensing head. The taper can sometimes be approximated by two fiber sections with different diameters. This approximation is valid when considering a sensing head composed of fibers with different diameters but in the case of tapered fibers, it can also be very accurate. Even more so, if the taper transition region is short when compared with the long uniform taper waist (see Figure 2.5). In this case, we neglect the effect of the transition region and consider a section with the untapered diameter and a section with the taper waist diameter. This deduction for the strain sensitivity takes into account solely the contribution of length extension of the sensing head and neglects the contribution of the refractive index change.

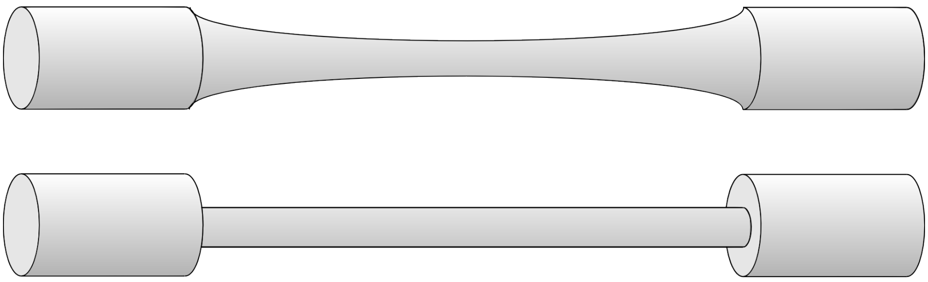

Figure 2.5 – Tapered fiber (top) and two diameters fiber equivalent (bottom).

Let us then derive an expression for the strain sensitivity of a tapered fiber structure assuming it is composed of two sections with different diameters: the tapered section's diameter and the original diameter [31].

The total length of fiber is given by $L_{total} = L_{taper} + L_{fiber}$. If stress is applied to the taper structure, at constant temperature, the wavelength will be shifted by $\Delta\lambda_{taper}$ according to:

$$\Delta\lambda_{taper} = \kappa_0 \varepsilon_{taper} \tag{2.1}$$

where κ_0 is a constant characteristic of the fiber material (which can be easily determined experimentally by analyzing the variation of the wavelength as a function of strain, at constant temperature) and ε_{taper} is the strain applied to the taper region. This is certainly a linear approximation where higher order terms are neglected.

However, if the strain is applied to the entire sensor, then an unequal load of stress will appear along each section of the sensor depending on the mechanical resistance. In particular, the strain loads applied to the fiber and the fused taper are related according to:

$$\varepsilon_{fiber} E A_{fiber} = \varepsilon_{taper} E A_{taper} \tag{2.2}$$

where E is the Young modulus of the sensor material and A_i ($i =$ fiber or taper) is the cross-sectional area of the fiber in the untapered and tapered regions, respectively. It is assumed that the mechanical properties of the material in both fiber and taper regions are the same. Consequently, the strain applied to the two sensor sections and the cladding diameters are related according to:

$$\frac{\varepsilon_{fiber}}{\varepsilon_{taper}} = \frac{d_{taper}^2}{d_{fiber}^2} \tag{2.3}$$

where d_{fiber} and d_{taper} are the cladding diameters of the fiber and taper, respectively. The longitudinal strain of the fused taper and piece of fiber are given by:

$$\varepsilon_{taper} = \frac{\Delta L_{taper}}{L_{taper}} \quad \text{and} \quad \varepsilon_{fiber} = \frac{\Delta L_{fiber}}{L_{fiber}} \tag{2.4}$$

where L_{taper} and L_{fiber} are the length of the sensor sections and ΔL_{taper} and ΔL_{fiber} are the extension of the taper and the fiber, respectively. By definition, the total longitudinal strain of the sensing head is given by:

$$\varepsilon_0 = \frac{\Delta L_{taper} + \Delta L_{fiber}}{L_{taper} + L_{fiber}} \tag{2.5}$$

Combining equations 2.3-2.5, it is possible to derive the ratio of strain in the taper (ε_{taper}) to the total strain (ε_0):

$$\varepsilon_{taper}/\varepsilon_0 = \frac{L_{fiber} + L_{taper}}{L_{fiber}\frac{d_{taper}^2}{d_{fiber}^2} + L_{taper}} \tag{2.6}$$

or the ratio of strain in the fiber to the total strain:

$$\varepsilon_{fiber}/\varepsilon_0 = \frac{L_{fiber} + L_{taper}}{L_{fiber} + L_{taper}\frac{d_{fiber}^2}{d_{taper}^2}} \tag{2.7}$$

Substituting equation 2.6 into equation 2.1, the wavelength shift can be rewritten as:

$$\Delta\lambda_{taper} = \kappa_0 \frac{L_{fiber} + L_{taper}}{L_{fiber}\frac{d_{taper}^2}{d_{fiber}^2} + L_{taper}} \varepsilon_0 \tag{2.8}$$

where the strain sensitivity related to the total strain applied to the sensing head will be given by:

$$\kappa_{taper} = \kappa_0 \frac{L_{fiber} + L_{taper}}{L_{fiber}\frac{d_{taper}^2}{d_{fiber}^2} + L_{taper}}, \text{ or} \tag{2.9}$$

$$\kappa_{taper} = \kappa_0 \cdot {}^{\varepsilon_{taper}}/_{\varepsilon_0} \tag{2.10}$$

The final strain sensitivity is thus given by the initial strain sensitivity κ_0 affected by the taper strain ratio. Equations 2.6 and 2.7 are represented graphically in Figures 2.6 and 2.7.

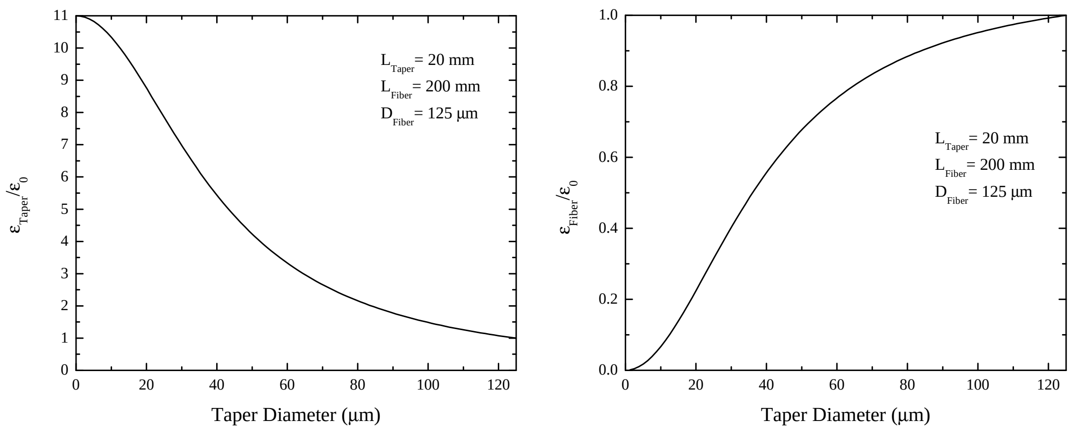

(a) $\varepsilon_{taper}/\varepsilon_0$ vs. d_{taper} **(b)** $\varepsilon_{fiber}/\varepsilon_0$ vs. d_{taper}

Figure 2.6 – Relationship between the strain ratios and the taper diameter.

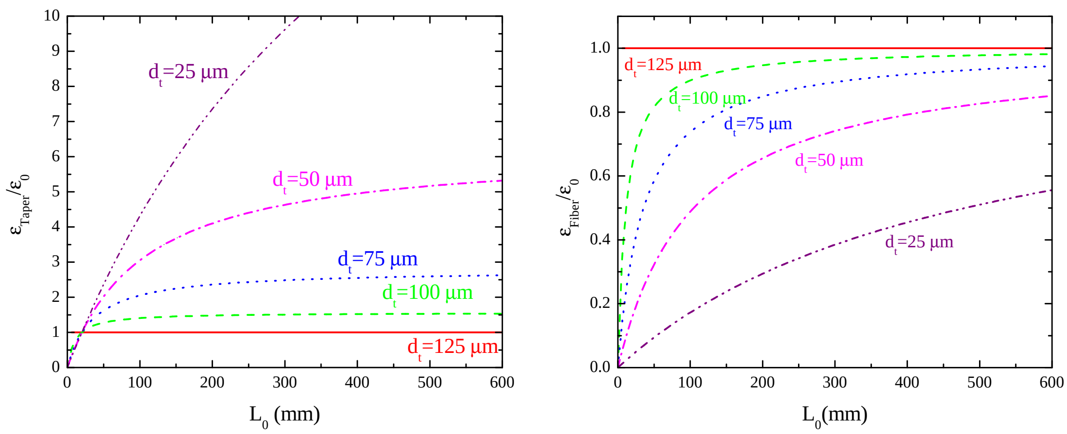

(a) $\varepsilon_{taper}/\varepsilon_0$ vs. L_0 ($L_{taper} = 20\,\text{mm}$) **(b)** $\varepsilon_{fiber}/\varepsilon_0$ vs. L_0 ($L_{taper} = 20\,\text{mm}$)

Figure 2.7 – Relationship between the strain ratios and the sensing heads' total length.

One thing readily observed in Figure 2.6 is that both ${}^{\varepsilon_{\text{taper}}}/_{\varepsilon_0}$ and ${}^{\varepsilon_{\text{fiber}}}/_{\varepsilon_0}$ are equal to unity when $d_{taper} = d_{fiber} = 125\,\mu\text{m}$. When we reduce the taper diameter (d_{taper}), the taper strain ratio increases while the fiber strain ratio decreases. This will lead to an increase in strain sensitivity in accordance with equation 2.10.

Figure 2.7 shows that both ratios have an asymptotic regime into a steady state (constant ratio). But, the smaller the taper waist, the longer the sensing head has to be in order to reach this state. This means that, especially for small taper diameters, the length of the total fiber head subjected to strain is a determining factor when calculating the sensitivities. Therefore, the total length should be kept as constant as possible when it is not a variable.

This analysis is very important and will be applied to several structures. It will be applied when considering tapers in coreless fiber working as multimode interference devices (Chapter 3), tapered long period gratings (Chapter 4), and tapers in suspended core fiber (Chapter 5 and 6).

Chapter 3

Tapers in Multimode Interference Devices

3.1 Introduction

Multimode interference (MMI) has been thoroughly investigated and many applications, namely in integrated optics, have sprouted from such concept. Self-imaging of the input light field has led to the development of directional couplers, beam splitters, and multiplexers just to name a few [32]. Multimode interference can also be obtained in optical fibers using a step-index multimode fiber (MMF) and can be used for optical communication and sensing [33]. The most usual form of an MMI-based optical fiber device consists of a multimode fiber section spliced between two single-mode fibers (SMF) forming an SMF-MMF-SMF structure (SMS) [34]. SMS fiber structures have been employed as many optical devices such as a displacement sensor [35], a fiber lens [36], refractometer sensors [37], bandpass filters [38], and edge filters [39]. Recently, Wang *et al.* proposed and experimentally demonstrated a high sensitivity evanescent field fiber refractometer based on a tapered multimode-single-mode fiber structure [40].

This chapter presents a tapered SMS structure that acts as a multimode interference device. The sensing head is composed of a 50 mm-long section of coreless multimode fiber, spliced between two SMF 28 fibers. On the coreless multimode section, tapers with different cross section diameters ranging from the untapered 125 μm to 15 μm were fabricated. Simulations of a conventional SMS structure and one that includes a taper in the multimode region were compared. Different SMS sensing heads with different taper dimensions were characterized in strain and temperature.

A simultaneous strain and temperature sensing configuration is also explored.

3.2 Fabrication and Characterization

3.2.1 Sensing Head Fabrication

The tapered Single-mode - Multimode - Single-mode (SMS) fiber structures were produced by Claudecir Biazoli at UNICAMP specifically for this work. Initially a piece of coreless multimode silica fiber with 125 μm diameter was spliced between two single-mode optical fibers. On the coreless multimode fiber, a taper was produced by the flame-brushing technique. This technique employs a flame that is swept along the fiber while it is being stretched and thus leads to the reduction of the transverse cross-section and the creation of a taper (see Figure 3.1). A computer controls the stretching and the flame-brushing, and allows for very accurate control of the taper shape.

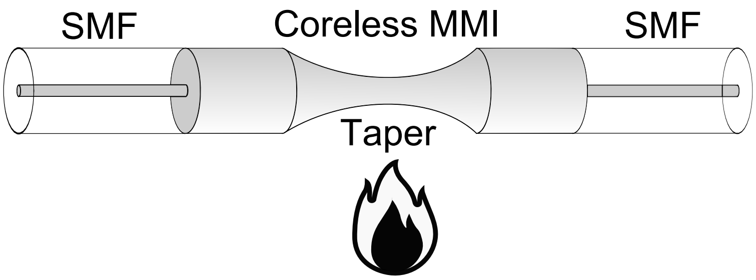

Figure 3.1 – SMS structure with a tapered multimode fiber section.

3.2.2 Strain and Temperature Characterization

For strain characterization, one end of the sensing head was fixed and the other was attached to a micrometric translation stage. Gradual stress was applied to the structure and the spectral response was monitored. The total length of the sensing head (400 mm) was subjected to strain. To determine the wavelength variations, the wavelength change of the main peaks was monitored through an optical spectrum analyzer with a maximum resolution of 0.05 nm.

For temperature characterization, the setup used is shown in Figure 3.2. The sensing head is inserted in a cylindrical oven and a constant stress is applied to it. This is done by fixing the fiber on one end and placing a weight on the other end. This way, the only variable is the temperature. Also, the refractive index change of air in the temperature range considered is negligible.

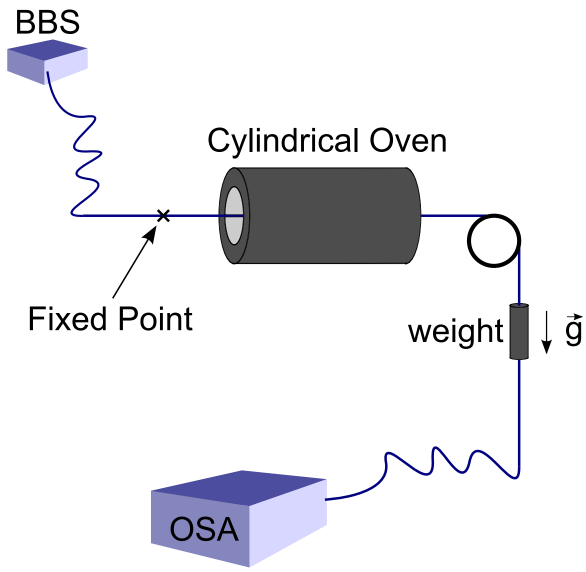

Figure 3.2 – Temperature characterization setup.

3.3 Theoretical and Experimental Results

3.3.1 Simulations

In Figure 3.3, simulations of an untapered MMF (a) and of the MMF tapered down to 55 μm (b) are presented. The simulation was performed using a Beam Propagation Method (BPM) for 3D propagation. The parameters used in the simulation are light injected at 1550 nm, 50 mm-long section of 125 μm coreless fiber with a refractive index of 1.444. In Figure 3.3a one can see the usual MMI pattern along the 50 mm of coreless fiber. In Figure 3.3b, it is evident that even though the taper changes the propagation of light inside the fiber, the MMI pattern is still clearly visible.

Analyzing with more care the tapered SMS simulation, it is easy to see that the self-images that result from multimode interference are more closely packed in the taper region. This means that when we apply strain to the tapered SMS structures the change in the output field is expected to be much greater that in the untapered case. This should in principle lead to a much larger strain sensitivity.

3.3.2 Spectral Response Analysis

When analyzing the spectral responses of SMS structures with different taper waists, one can identify, for small diameter reduction (large taper waists), a clear MMI image in the spectrum (see Figure 3.4a and 3.4b). As the taper waist is reduced a smaller number of propagating modes is expected. This is seen in Figure 3.4b because a larger

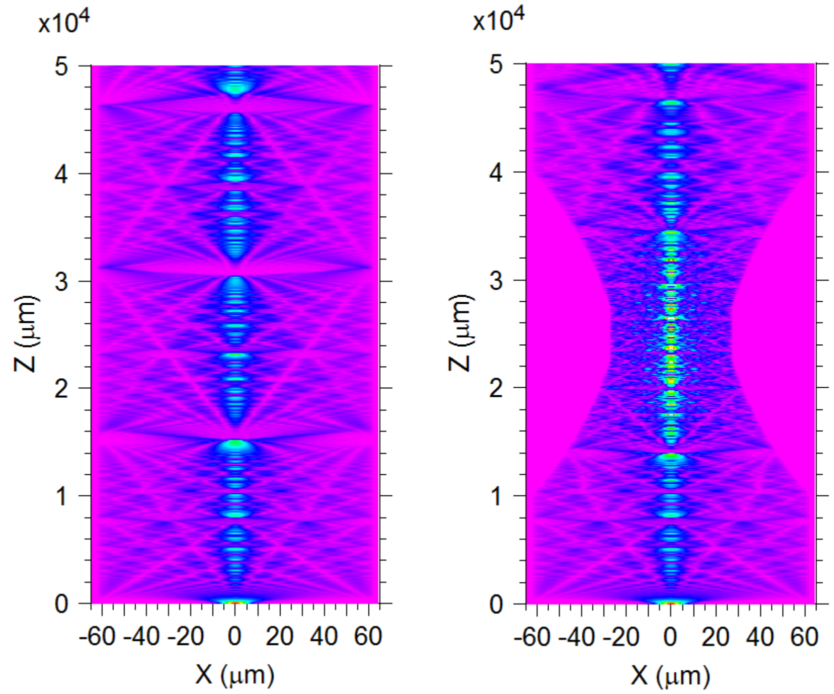

(a) Untapered **(b)** Tapered down to 55 μm

Figure 3.3 – 3D BPM calculated electric field amplitude distribution in the XZ plane of a coreless MMF.

bandwidth is visible which results from a smaller number of modes. When going to smaller taper waists (25 μm and 15 μm), the number of modes that propagate through the taper region should be even smaller but the intermodal interference present does not allow us to take such conclusions (Figures 3.4c and 3.4d).

3.3.3 Strain Characterization

Figure 3.5 shows the wavelength shifts corresponding to the applied strain for each SMS structure. As the taper diameter decreases, the sensing heads' strain sensitivity increases. The wavelength shift due to applied strain is given by:

$$\Delta\lambda = \kappa_\epsilon \Delta\varepsilon \tag{3.1}$$

where $\kappa_\varepsilon = {}^{\partial\lambda}/_{\partial\varepsilon}$ is a material parameter related to the Poisson ratio, the photoelastic constant and the effective refractive index. A blue shift is visible from Figure 3.5. It derives from the dominance of the photoelastic effect over the extension of the fiber. In fact, the length of the fiber is too short for the extension to be dominant.

In Figure 3.6 the strain sensitivities for SMS structures with tapers widths of

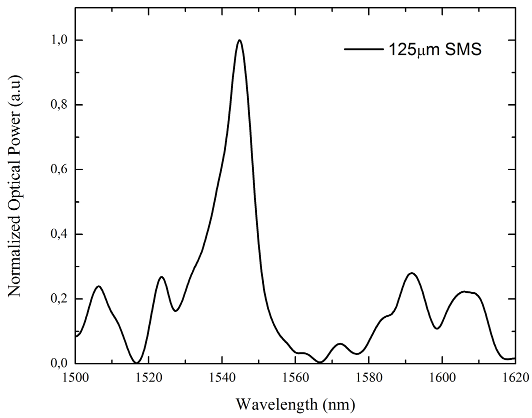

(a) 125 μm untapered SMS structure.

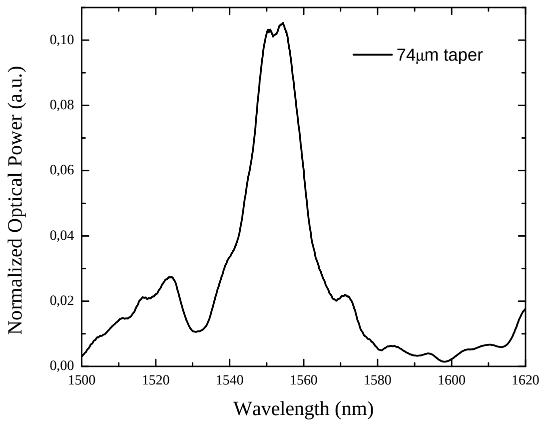

(b) 74 μm tapered SMS structure.

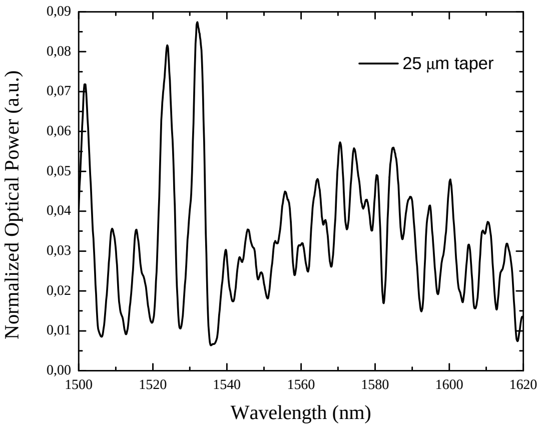

(c) 25 μm tapered SMS structure.

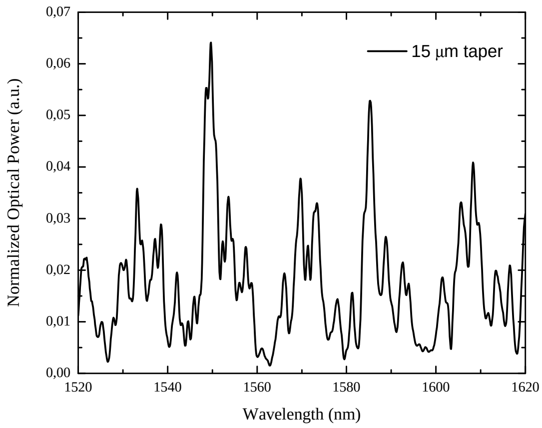

(d) 15 μm tapered SMS structure.

Figure 3.4 – Spectral responses of several tapered SMS structures.

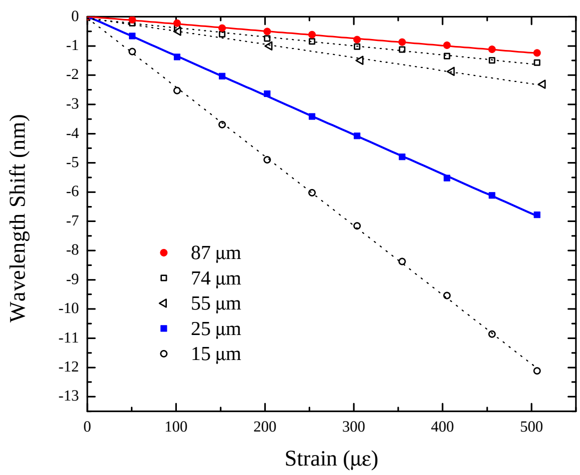

Figure 3.5 – Relationship between the wavelength shift and the applied strain for several tapered SMS structures. In full are the two sensing heads used in the simultaneous strain and temperature sensing (sensitivities in bold in Table 3.1).

125 μm, 87 μm, 74 μm, 55 μm, 25 μm, and 15 μm are plotted (the actual values are presented in Table 3.1). The theoretical expression plotted in Figure 3.6 is given by equation 2.9 which results from the analysis present in Chapter 2.3. Strain sensitivity varies nonlinearly with taper waist diameter. Sensitivities of $-2.48\,\mathrm{pm}/\mu\varepsilon$ and $-13.5\,\mathrm{pm}/\mu\varepsilon$ were obtained for the 87 μm and 25 μm tapered SMSs. A tenfold increase in strain sensitivity was achieved when tapering the SMS structure from 125 μm ($-2.08\,\mathrm{pm}/\mu\varepsilon$) to 15 μm ($-23.69\,\mathrm{pm}/\mu\varepsilon$).

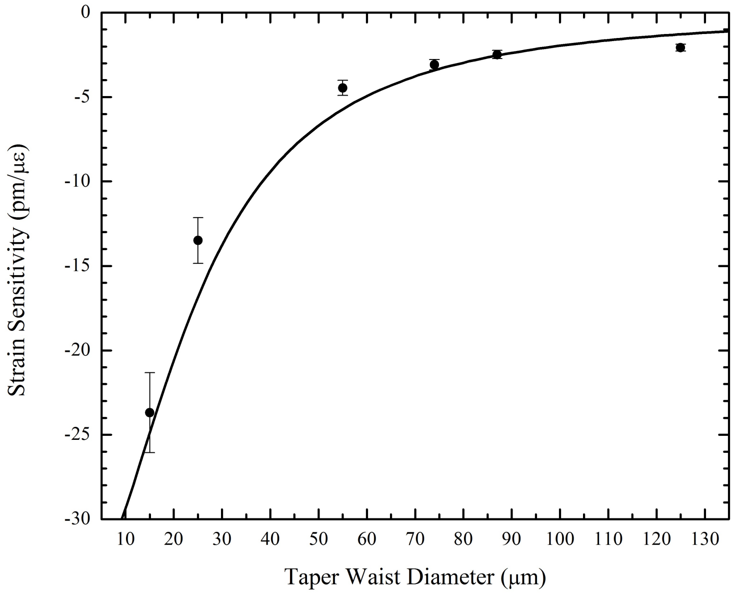

Figure 3.6 – Relationship between strain sensitivity and taper diameter. Experimental results and fitting to the theoretical expression.

Taper Diameter (μm)	Strain Sensitivity ($\mathrm{pm}/\mu\varepsilon$)
125	-2.08
87	**-2.48**
74	-3.09
55	-4.45
25	**-13.5**
15	-23.7

Table 3.1 – Strain sensitivities of different taper diameters. In bold are the two tapers considered in the simultaneous measurement of strain and temperature.

3.3.4 Temperature Characterization

As for temperature, the sensing heads have slightly different sensitivities, namely 16.56 pm/K for the 87 μm taper and 13.95 pm/K for the 25 μm taper (see Figure 3.7). A red shift occurs when temperature increases which means that the dominant parameter is thermal expansion. Also, as seen in Figure 3.8, sensitivity decreases as taper diameter is decreased.

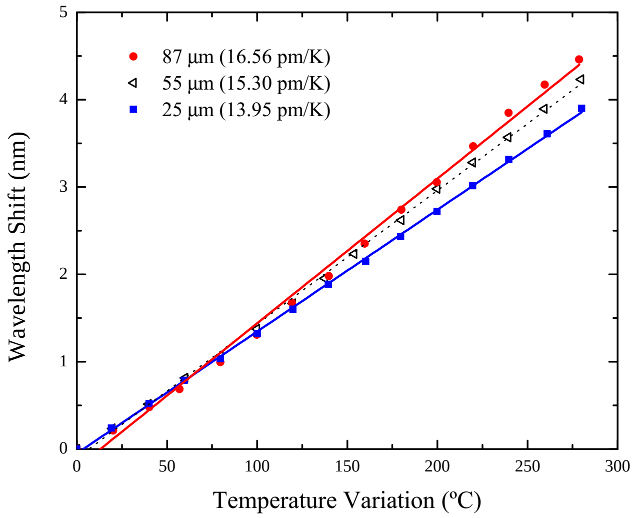

Figure 3.7 – Relationship between the wavelength shift and temperature variation for several tapered SMS structures.

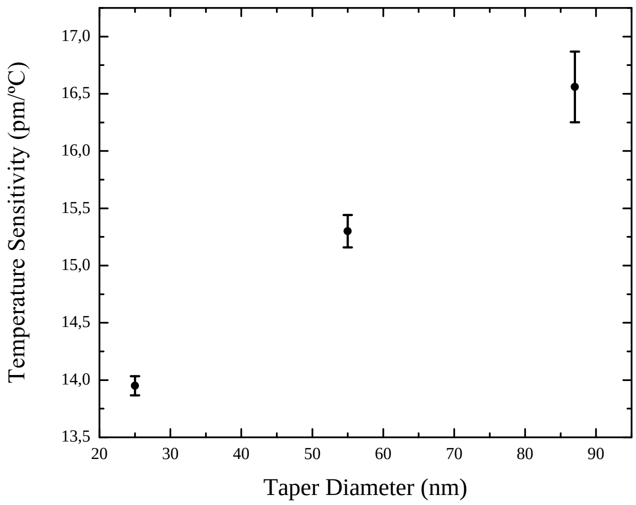

Figure 3.8 – Relationship between temperature sensitivity and taper diameter.

3.4 Simultaneous Measurement of Strain and Temperature

In this section, a proof of concept for the simultaneous measurement of strain and temperature is presented using the tapered SMS structures. These tapered SMS structures can be used for simultaneous measurement of temperature and strain using two different diameter tapers. A solution is presented using the matrix method. Considering two different tapered SMS structures, namely the ones tapered down to 87 μm and 25 μm one has:

$$\Lambda = [K]\,\Omega \text{ or equivalently}$$

$$\begin{bmatrix} \Delta\lambda_{(87)} \\ \Delta\lambda_{(25)} \end{bmatrix} = \begin{bmatrix} \kappa_{T(87)} & \kappa_{\varepsilon(87)} \\ \kappa_{T(25)} & \kappa_{\varepsilon(25)} \end{bmatrix} \begin{bmatrix} \Delta T \\ \Delta\varepsilon \end{bmatrix} \tag{3.2}$$

where κ_T and κ_ε are the sensitivities to temperature and strain.

Inverting the matrix expressions for the temperature and strain variations as a function of the sensitivities and wavelength shifts one can obtain:

$$\begin{bmatrix} \Delta T \\ \Delta\varepsilon \end{bmatrix} = \frac{1}{D} \begin{bmatrix} \kappa_{\varepsilon(25)} & -\kappa_{\varepsilon(87)} \\ -\kappa_{T(25)} & \kappa_{T(87)} \end{bmatrix} \begin{bmatrix} \Delta\lambda_{(87)} \\ \Delta\lambda_{(25)} \end{bmatrix} \tag{3.3}$$

where $D = \kappa_{T(87)}\kappa_{\varepsilon(25)} - \kappa_{\varepsilon(87)}\kappa_{T(25)}$. The limitation of most methods reported for simultaneous measurement of pairs of quasi-static parameters arises from a small value of the matrix determinant [41], which makes it highly sensitive to noise. The configuration is substantially immune to this problem when the difference of the sensitivity slopes of the two SMS structures is large. From the values given in Figures 3.5 and 3.7, equation 3.3 becomes:

$$\begin{bmatrix} \Delta T \\ \Delta\varepsilon \end{bmatrix} = -\frac{1}{189.0} \begin{bmatrix} -13.50 & 2.48 \\ -13.95 & 16.56 \end{bmatrix} \begin{bmatrix} \Delta\lambda_{(87)} \\ \Delta\lambda_{(25)} \end{bmatrix} \tag{3.4}$$

The performance of this simultaneous measurement configuration was experimentally determined by undertaking strain variations in a range of 500 $\mu\varepsilon$ at a fixed temperature (140 °C) and the other way around, i.e., temperature variations in a

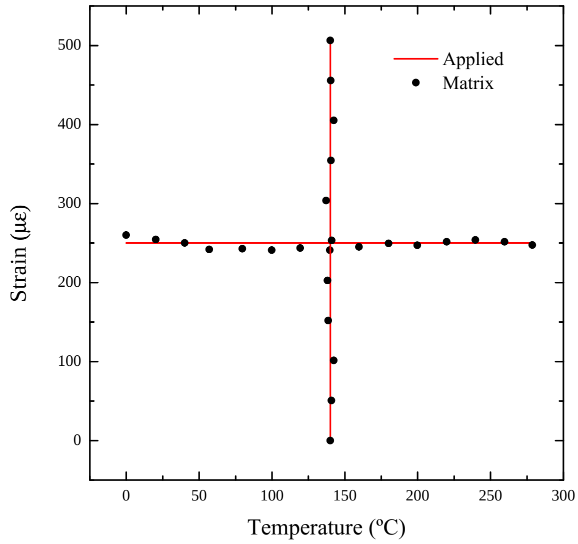

Figure 3.9 – Sensor output as determined by equation 3.4 for an applied strain at constant temperature, and a temperature variation at constant strain.

range of 280 °C for a specific applied strain ($\Delta\epsilon = 250\,\mu\varepsilon$). The results are expressed in Figure 3.9, where maximum errors relative to the applied values appear. From these results, resolutions of $\pm 1.6\,°\mathrm{C}$ and $\pm 5.6\,\mu\varepsilon$ were determined for temperature and strain measurements, respectively.

Besides determining the resolutions, it is necessary to determine the stability of the sensitivity matrix. Stability can be verified through the condition number of the matrix, which is an algebraic quantity that provides a qualitative estimate for the sensitivity of the solution of a system of linear equations [41].

The condition number is given by:

$$\text{Condition } \# = \|K\|_2 \left\|K^{-1}\right\|_2$$

where $\|K\|_2$ is the matrix 2-norm of K and is given by

$$\|K\|_2 = \sqrt{\text{largest eigenvalue of } K^{*}K}.$$

The larger the condition number of the matrix, the larger the upper bound for the relative error. Consequently, for matrices with high condition number, a small relative error in $[\Lambda]$ can lead to a large relative error in the solution $[\Omega]$. In order to have a well-conditioned system, cross-sensitivity between the two sensors is necessary, i.e., the one with higher temperature sensitivity must be the one with the lowest strain sensitivity. That is the case with the sensors considered. The condition number obtained is 3.16. It is interesting to determine the relative performance of several configurations using the matrices' condition number (see Table 3.2). To the author's knowledge, the sensing configuration presented has the lowest condition number when considering dual-parameter sensing of strain and temperature. The sensing configuration that gets the closest, with a condition number of 5.5, monitors the wavelength of an FBG sensor and the frequency of the Brillouin gain spectra over a 20 m fiber length [42].

Sensing Configuration	Condition Number	Reference Number
Type IA/IIA	55.3	[43]
FBG + MMF	45.0	[44]
Tilted FBG	39.4	[45]
FBG in Taper	26.4	[17]
Bragg Fibers	21.3	[46]
FBG in MOF	15.3	[47]
FBG + Brillouin	5.50	[42]
Tapered SMS structures	**3.16**	**This work [48]**

Table 3.2 – Inversion matrix condition number for several sensing configurations.

3.5 Discussion

Tapers were produced on SMS structures and were characterized in strain. From the simulations it was ascertained that the creation of a taper in the MMF section of the SMS does not destroy the MMI pattern. In fact, what happens is that the self-images appear more closely packed in the taper region. Because of this, an increase of strain sensitivity was expected and confirmed since stretching the taper will lead to a greater shift in the MMI pattern and consequent change in output light field. A ten-fold increase in strain sensitivity was achieved when tapering the SMS structure from 125 μm ($-2.08\,\mathrm{pm}/\mu\varepsilon$) to 15 μm ($-23.69\,\mathrm{pm}/\mu\varepsilon$). Combining two SMS structures, for example, one untapered and one tapered, it is possible to measure strain and temperature simultaneously. Resolutions of $\pm 1.6\,^{\circ}\mathrm{C}$ and $\pm 5.6\,\mu\varepsilon$ were achieved.

Chapter 4

Tapered Long Period Gratings

4.1 Introduction

Long period gratings (LPGs) are periodic variations in the fiber core refractive index that induce a spectral loss spectrum response. This periodic perturbation allows the coupling of light from an optical core mode to co-propagating cladding modes. LPGs in optical fibers have many applications both in optical communication as band-reject filters for amplifier equalization [49], or in optical sensing for multi-parameter measurement [50]. LPGs are interesting devices for sensing due to the fact that attenuation bands are very sensitive to different physical parameters such as temperature, strain, curvature, pressure and refractive index of liquids [51, 52]. It is also possible to combine this device with others such as FBGs [53] or even with another LPG in series [54]. The combination of LPGs with a taper has recently become a subject of study, mainly for the development of high sensitivity sensors. Highly sensitive refractive index sensors have been demonstrated either by combining an LPG pair with a taper [55] or using a tapered LPG device [56]. Tapered long period gratings written on conventional [57] or photonic crystal fiber [58] have also been used for pressure sensing. Another solution that was proposed was an optical inclinometer combining a taper in series with an LPG [9].

In this chapter, the fabrication of an LPG on the tapered region of a standard optical fiber (SMF 28) is used to obtain ultra-high strain sensitivity. Three configurations were produced, studied and compared: an LPG written in the conventional SMF 28 fiber, an LPG in series with a taper, and an LPG written in the taper region.

4.2 Fabrication and Characterization

Cladding modes have large optical attenuation, hence, when measuring the transmitted signal as a function of wavelength one obtains several attenuation bands, each one at a different spectral position and related to a particular cladding mode. The spectral location of the band can be obtained by $\lambda = \Delta n \times \Lambda$, where λ is the resonant wavelength, Δn is the difference between core and cladding modes' effective refractive indices, and Λ is the grating's period, i.e., the distance between fiber perturbations. When strain (ε) is applied to the fiber, it will stretch and the periodicity of the grating will change, as will the refractive index. Consequently, the resonant wavelength will suffer a wavelength shift. Through the measurement of the band position one can thus measure the strain applied to the fiber.

The wavelength shift that results when strain is applied to the LPG sensor is given by $\Delta\lambda_{LPG} = \kappa\varepsilon$, where κ depends on the geometric and optical properties of the LPG, the fiber material and the optical mode. Just like explained in Chapter 2.3, the application of strain to a fiber with uniform diameter results in a uniform strain distribution along the fiber. But if the fiber has two different diameters, the unperturbed and the tapered regions, the strain will be different at different points along the fiber. Two distinct tensions will exist: one in the original diameter fiber resulting in ε_F, and the other in the tapered section resulting in ε_T, with ε_0 being the integrated strain over the fiber length L_0. This way, if the LPG is written on the tapered region, as schematically shown in Figure 4.1, a strain sensor with higher strain sensitivity is achievable.

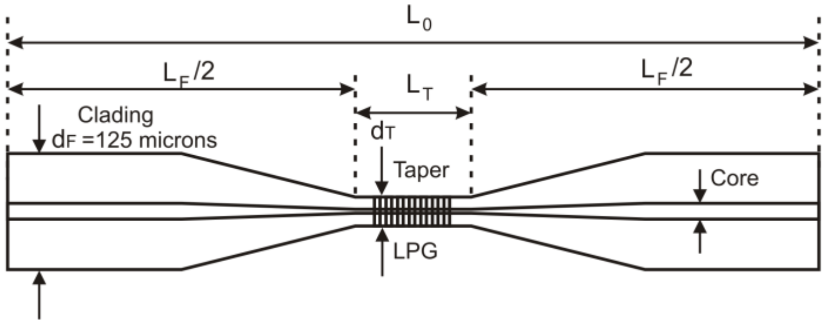

Figure 4.1 – Sensing head structure based on an LPG, written on the taper region.

4.2.1 Sensing Head Fabrication

The three different sensing heads fabricated are presented in Figure 4.2:

a) An LPG with a periodicity of 600 μm was fabricated on the tapered region of a fiber.

b) An LPG written on a conventional single mode fiber (SMF 28).

c) An LPG written on the untapered region in series with a taper. The total length of these last two structures is equal to the length of the first structure, i.e. 150 mm.

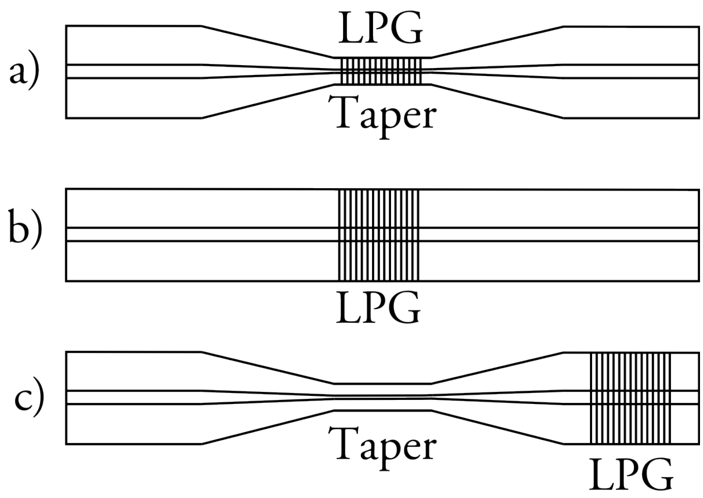

Figure 4.2 – Three different LPG sensing head configurations used in this work.

4.2.2 Strain Characterization

For sensing head a), a main loss peak was observed at 1530 nm. The taper has a waist of 20 μm and a length of 10 mm. The total length of the sensing head (L_0) is 150 mm. A blue shift was obtained when applying strain to the tapered LPG structure. This response can be seen in Figure 4.3 and has a behavior similar to that of normal LPGs written with CO_2 lasers [4].

For the situation of an LPG written in SMF 28 fiber (sensing head b), the strain sensitivity was measured to be $-0.90\,\mathrm{pm}/\mu\varepsilon$ (see Figure 4.4). This is the κ value of the equation in section 4.2. When a taper is fabricated in series with the previous LPG (sensing head c), a reduced sensitivity arises due to the nonuniform distribution of strain. A strain sensitivity of $\alpha = -0.23\,\mathrm{pm}/\mu\varepsilon$ was obtained which corresponds to the κ value of this grating times a factor given by equation 2.7:

$$\varepsilon_{fiber}/\varepsilon_0 = \frac{L_{fiber} + L_{taper}}{L_{fiber} + L_{taper}\frac{d^2_{fiber}}{d^2_{taper}}}$$

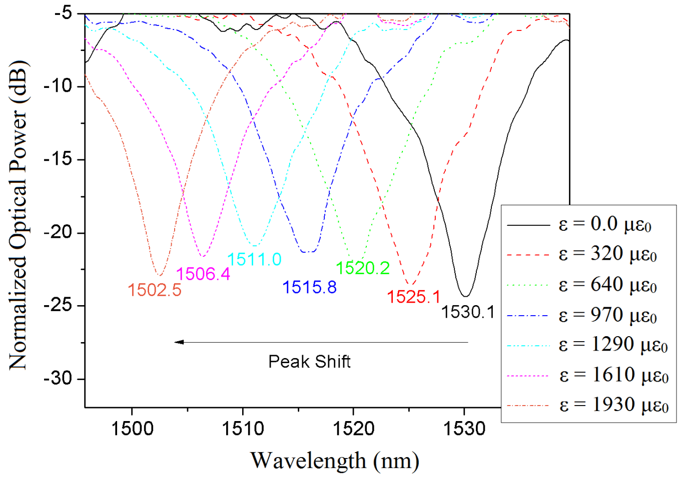

Figure 4.3 – Band shifts for several values of applied strain. In this case, the LPG was written on a taper with a diameter of $20\,\mu$m, $L_0 = 150\,$mm and $L_T = 10\,$mm.

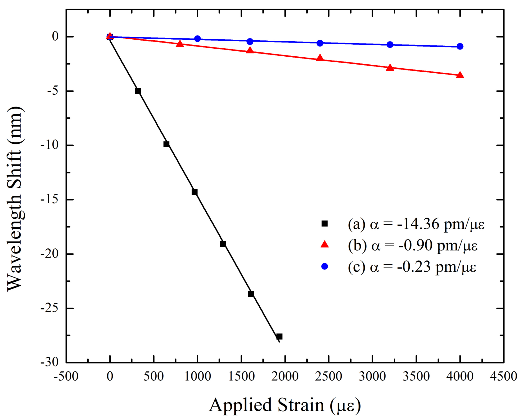

Figure 4.4 – Study of the strain sensitivity for each sensing head. Taper diameter is $20\,\mu$m, $L_0 = 150\,$mm and $L_T = 10\,$mm.

It should be noted that, as both gratings are identical and recorded over exactly the same fiber (sensing heads b and c), their κ factors should be the same.

To compare the experimental sensitivity obtained for sensing head c ($\alpha = -0.23\,\mathrm{pm}/\mu\varepsilon$) with the expected one, the $\varepsilon_F/\varepsilon_0$ ratio is calculated to be 0.28. By multiplying this ratio by the LPG κ value one obtains $-0.25\,\mathrm{pm}/\mu\varepsilon$, in good approximation with the experimental value.

As expected, in the case of the LPG written on the tapered region (sensing head a), the sensing head has larger strain sensitivity ($-14.36\,\mathrm{pm}/\mu\varepsilon$). Using the fiber data and with the help of equation 2.6, $\varepsilon_T/\varepsilon_0$ can be found to be 11.04. In this situation the κ value in unknown - and expected to be considerably different from the previous one as the grating is now written in a very different fiber.

All these three structures were characterized with the same total fiber length of 150 mm. A dependence of the strain sensitivity on the total fiber length was, however, also analyzed and is shown in Figure 4.5. For an LPG written on the tapered region and L_0 varying from 290 mm to 560 mm, the strain sensitivity was measured to change from $-16.8\,{}^{\text{pm}}/_{\mu\varepsilon}$ to $-24.8\,{}^{\text{pm}}/_{\mu\varepsilon}$.

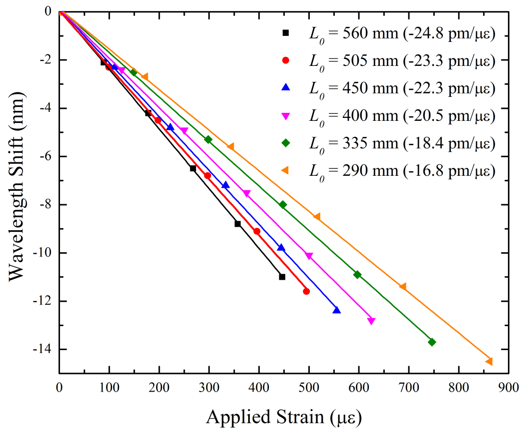

Figure 4.5 – Study of the strain sensitivity as a function of the total fiber length. The sensing head is the same as in the first case above (a).

4.3 Discussion

LPGs were produced on optical fiber tapers and very high strain sensitivities were attained when compared to LPGs written on conventional single mode fiber. This enhanced sensitivity occurs because strain is not equally distributed in a tapered fiber – in such situation the thinnest region is the most strained region. Therefore, an LPG produced in the taper region will have a much higher sensitivity, as demonstrated. Enhancements of an order of magnitude were achieved. When studying the sensitivity variation of such structure with total fiber length (length of fiber subjected to strain) an increase in sensitivity is observed for longer fibers. This was expected because the longer the fiber, the larger the strain ratio $({}^{\varepsilon_T}/_{\varepsilon_0})$ on the taper section. Important to note the same concept of using fibers with different diameters along its length can also be applied with other fiber strain sensing devices other than LPGs.

This study can also be explored for simultaneous measurement of, e.g., strain and temperature. In this case, the sensing head could consist of two LPGs written on tapered and untapered regions with different loss peak wavelengths. Different strain sensitivities are then expected but with similar response to temperature. Other possible applications are to use these filters as interrogation systems.

Chapter 5

Suspended Core Fiber Tapers

5.1 Introduction

Since Knight *et al.* [1] introduced, in 1996, microstructured optical fibers (MOFs) to the scientific community, they have found applications in all kinds of areas, from optical communication to optical sensing. Microstructured optical fibers are fibers that have a structure of air holes that run along the whole length of the fiber, and because of this, they present extraordinary properties. Some, instead of air holes may have rods with different materials and refractive indices.

A common geometry is the suspended core structure, where relatively large air holes surround the fiber core, giving the impression that the core is suspended along the fiber axis by thin silica bridges (see Figure 5.1). This fiber was first proposed and demonstrated by Monro *et al.* [59] in 2001. The core had $1\,\mu$m diameter and an estimated 17% of the fundamental mode power was located in the air at 1550 nm. This immediately suggested its use as an evanescent field sensor. Webb *et al.* [60] demonstrated a basic gas sensor for acetylene. Suspended core fibers can be used for supercontinuum generation due to their strong confinement of light in the core [21], and polymer SCFs have been demonstrated for low-loss terahertz guidance [61].

Over the last decade, the tapering of microstructured optical fibers has been improved [62, 63], and very interesting optical microstructures have been developed. It was shown that microstructured optical fibers could be tapered while retaining their cross-sectional profiles with little or no distortion [64]. The cross-sectional profile could thus be scaled down proportionally producing structures with very small core diameters. Mägi *et al.* [64] were the first to achieve a pitch below 300 nm in a tapered MOF. Tapered MOF sensors as temperature-independent strain sensors were also reported [22].

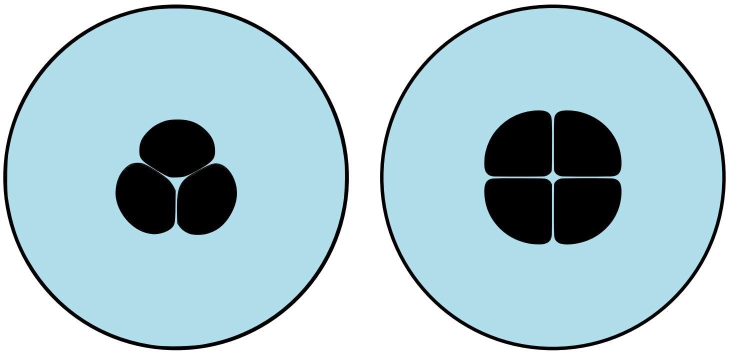

(a) Three hole SCF (b) Four hole SCF

Figure 5.1 – Different Suspended Core Fibers.

Nonetheless, the tapering of suspended core fiber has not been explored for sensing applications. Few references can be found in the literature on tapering this type of fiber and they consist mainly on theoretical analyses or their application in supercontinuum generation.

5.2 Fabrication and Characterization

5.2.1 Taper Fabrication

The suspended core fiber (SCF) tapers used in this work were produced by Susana Silva at IPHT-Jena specifically for this line of investigation. Figure 5.2 illustrates the experimental setup used for the production of the SCF tapers. Tapers with several taper waist diameters (120 μm, 115 μm, 110 μm, 105 μm, 100 μm, 95 μm, 90 μm, 85 μm, 80 μm, 75 μm, 70 μm and 40 μm) were produced using a VYTRAN - glass processing workstation. As explained in section 2.2.1, the fiber is heated to its softening point while a tensile force is applied, thus creating the taper.

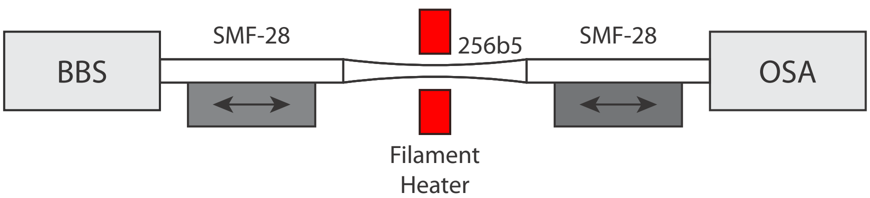

Figure 5.2 – Schematic experimental setup used to produce the SCF tapers (BBS - Broadband Source, OSA - Optical Spectrum Analyzer).

The tapers were fabricated on a suspended core fiber (IPHT) with 8.4 μm and 128 μm core and cladding diameters, respectively. This fiber has four holes with

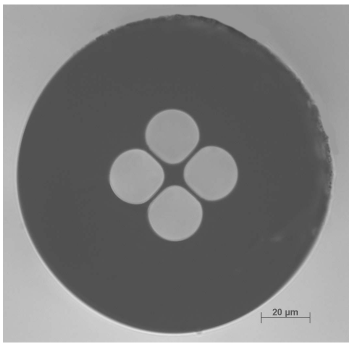

Figure 5.3 – Cross section micrograph of the Suspended Core Fiber.

diameters of 22 μm each and a bridge width of 1.5 μm (see Figure 5.3). 10 mm-long tapers were made in SCF sections that in turn were spliced between two single-mode fibers (SMF28). The SCF sections all have similar lengths between 25 mm to 30 mm. A broadband source in the 1550 nm spectral range, and an optical spectrum analyzer, were used to monitor in real time the tapering process.

5.2.2 Cross Section Characterization

In order to analyze the cross section of the tapers and evaluate the transverse profile of the tapers, they where cleaved at the taper waist after every other characterization was complete. They were then inspected using a transmission optical microscope at several magnifications. Photographs were taken for a posterior analysis.

5.2.3 Strain, Temperature and Refractometric Characterization

For strain characterization, a similar setup to that of Figure 5.2 was used. In this case, there was no microheater present and one end of the fiber was fixed. The total length of fiber that was subjected to strain was approximately 135 mm long, of which only between 25 mm to 30 mm were suspended core fiber, and only 10 mm of that length were tapered to different diameters. Much care was needed to transport and handle the sensing heads, not because of the taper regions themselves but because of the somewhat weak splices between the SCF and SMF 28. The data relating to the 75 μm and 95 μm tapers is missing because the splices did not endure the stress applied to them.

For temperature characterization, the whole sensing head (SCF section) was immersed in water to achieve an optimal equilibrium.

To determine if the sensing heads were sensitive to the surrounding medium's refractive index, they were immersed in ethanol which has a refractive index of 1.36.

In all these characterizations, the sensing structures were interrogated with a broadband source in the 1550 nm spectral range and analyzed in transmission with an optical spectrum analyzer with a maximum resolution of 0.1 nm.

5.3 Theoretical and Experimental Results

5.3.1 Simulations

The suspended core fiber shown in Figure 5.3 was simulated using a Beam Propagation Method (BPM) to obtain the modes supported by such structure. In Figure 5.5, the first four guided modes are represented. These modes are evidently orthogonal, but when they recombine at the output splice between the SCF and SMF they must be expanded in a different set of modes and they recombine with each other [65].

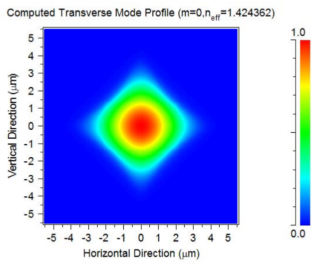

(a) m = 0

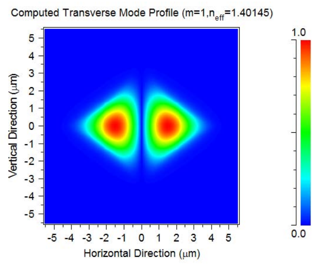

Figure 5.4 – m = 1

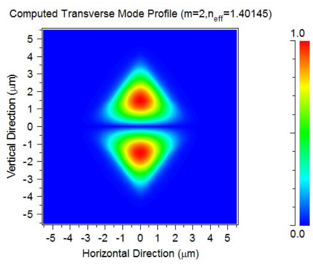

(a) m = 2

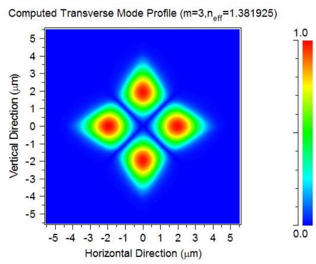

(b) m = 3

Figure 5.5 – BPM simulations of the four lowest order modes guided in the four-hole suspended core fiber.

The WKB method can be applied to a general graded-index fiber to determine the number of guided modes. Taking the step-index limit, a similar expression for these fibers can be obtained. When considering a graded-index fiber one usually defines its refractive index profile as:

$$\begin{cases} n(r) = n_1 \left[1 - 2\Delta \left(\frac{r}{a}\right)^{\alpha}\right]^{1/2} & (0 \leq r \leq a), \\ n_0 = n_1 (1 - 2\Delta)^{1/2} & (r > a), \end{cases} \tag{5.1}$$

where n_0 and n_1 are the cladding and maximum core refractive indices, a is the radius of the fiber, and α is a power coefficient assumed to range between 1 and ∞. Applying the WKB method to multimode graded-index fibers one obtains the following expression for the number of guided modes N:

$$N = \frac{\alpha}{\alpha + 2} k^2 n_1^2 \Delta a^2 = \frac{\alpha}{\alpha + 2} \frac{V^2}{2}, \tag{5.2}$$

where V is the normalized frequency, defined as $V = ka\sqrt{(n_1^2 - n_0^2)} = 2\sqrt{k^2 a^2 n_1^2 \Delta}$ [66]. Considering step-index fibers ($\alpha = \infty$), the number of guided modes results in

$$N = \frac{V^2}{2}. \tag{5.3}$$

This expression is valid for cylindrical (core and cladding) fibers with normalized frequencies (V) greater than 5 [66].

Figure 5.6 shows that the actual number of modes of the SCF structure does follow a quadratic tendency but it does not correspond to the expression previously stated. In fact, the number of modes follows an expression, derived from the quadratic fit of Figure 5.6, given by $N \approx V^2/5$. In the suspended-core fiber, the core diameter is taken to be the in-circle diameter of the suspended core. This can be compared with a standard graded-index fiber, where $\alpha = 2$, and consequently $N = V^2/4$. The coefficient of the quadratic function for the SCF is even lower than that of the graded-index fiber. It should be noted that this is a continuous approximation because the number of modes is obviously discrete.

5.3.2 Cross Section Analysis

One observes from Figure 5.7 that as the original SCF is tapered, both core and cladding diameters are reduced. The core geometry was maintained all through the process and, therefore, the waveguide suffered a uniform reduction maintaining the cross-sectional profile. Even at 32% of the original size, the holes do not collapse. The ratio between core and cladding diameters is $0.069 \pm 0.002\,\mu$m/μm. The core diameter reduces from the initial $8.4\,\mu$m ($125\,\mu$m cladding) to about $2.4\,\mu$m ($40\,\mu$m

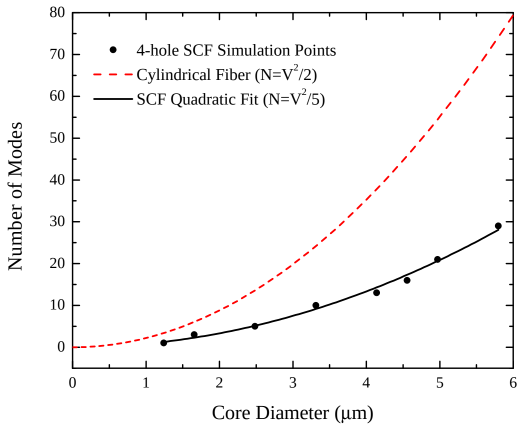

Figure 5.6 – Relationship between the number of modes and the core diameter of a suspended core four-hole fiber. Also included are a quadratic fit (solid) and the theoretical expression for cylindrical fibers (dashed).

cladding).

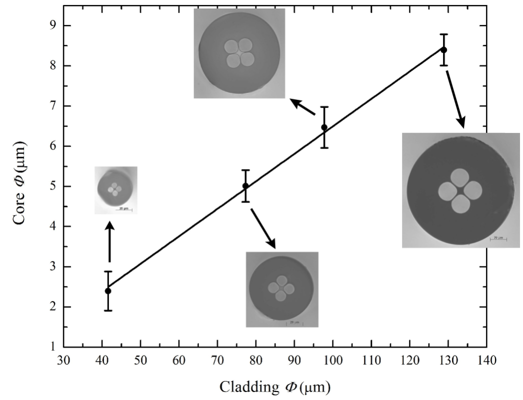

Figure 5.7 – Relationship between core and cladding diameters.

5.3.3 Spectral Response Analysis

As referred in Section 5.2.1, the spectral response was monitored before and after tapering the SCF. Before tapering, the sensing head acts as a multimode interference device – the light field propagating along the input SMF enters the SCF section and several modes are excited. This interference appears because different modes, which propagate along the SCF with different phase velocities, are recombined at the splice between SCF and singlemode fibers (see Figures 5.8a, 5.9a and 5.10a). For example, in the 70 μm case (Figure 5.10a), a well-defined notch peak at $\sim$ 1585 nm appears due to destructive interference between a few specific modes.

After tapering, the reduction in core diameter leads to the consequent reduction in the number of guided modes. Now, as the taper diameter gets smaller and smaller, the number of modes that propagate through the taper gets smaller and smaller, becoming more and more evident beating among only a few. This leads to intermodal interference between just a few modes. In Figure 5.10b, a beat is clearly visible for the 70 μm taper. As we go to larger taper waists, the beat gets less and less visible and for instance, for very little diameter reduction – 115 μm (Figure 5.8b) the beat is not evident.

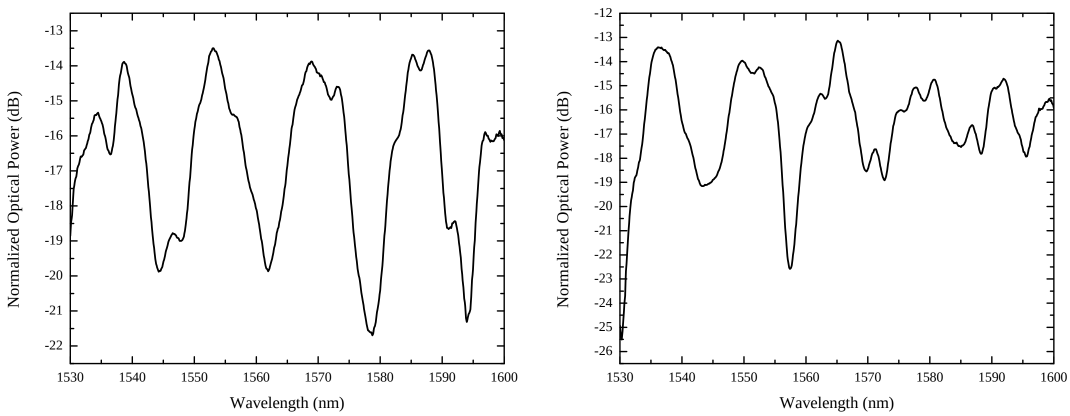

(a) Spectral response of SCF before tapering.

(b) Spectral response of SCF taper after tapering.

Figure 5.8 – Spectral response of the 125 μm SCF (pre-tapering) and the 115 μm SCF taper (post-tapering).

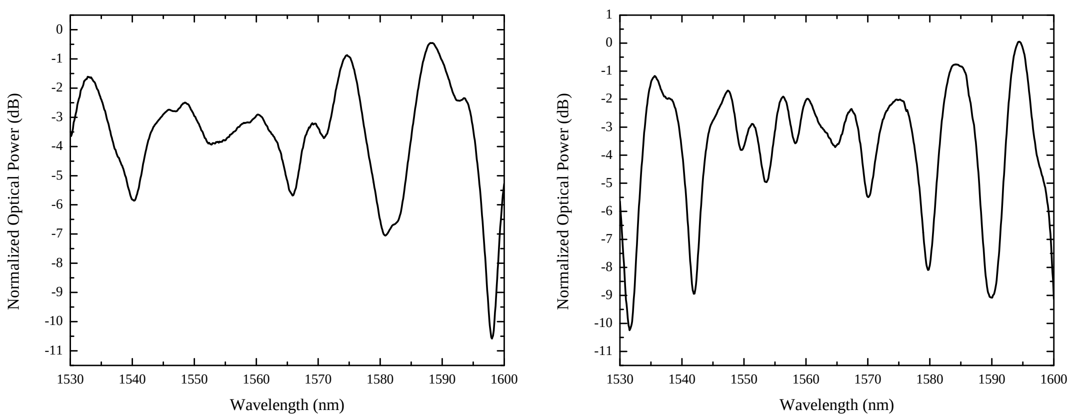

(a) Spectral response of SCF before tapering.

(b) Spectral response of SCF taper after tapering.

Figure 5.9 – Spectral response of the 125 μm SCF (pre-tapering) and the 95 μm SCF taper (post-tapering).

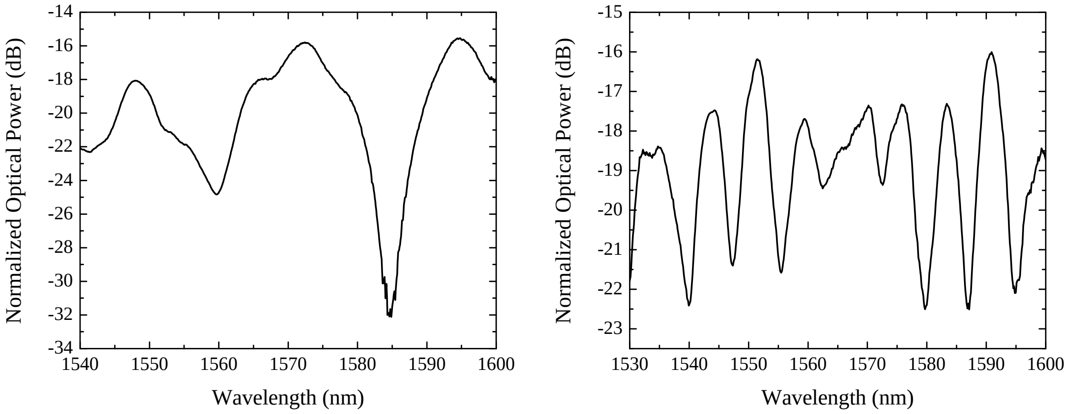

(a) Spectral response of SCF before tapering.

(b) Spectral response of SCF taper after tapering.

Figure 5.10 – Spectral response of the 125 μm SCF (pre-tapering) and the 70 μm SCF taper (post-tapering).

5.3.4 Strain Characterization

Figure 5.11 shows the different response curves for the wavelength change with applied strain for several taper waist diameters. A clear blue shift is observable for each taper response. This is because the elasto-optic effect is predominant over the length increase due to strain. The sensing head is too small for the length increase to be dominant.

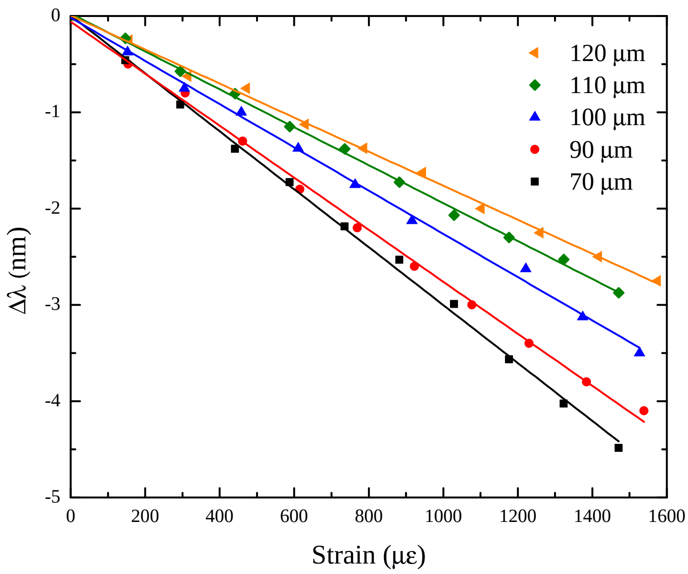

Figure 5.11 – Wavelength change with applied strain for the 70 μm, 90 μm, 100 μm, 110 μm and 120 μm tapers.

The strain sensitivity is in reality given by the strain sensitivity of the untapered fiber (κ_0) affected by a factor that is greater than one for a tapered fiber ($d_{taper} < d_{fiber}$). As d_{taper} becomes smaller, this multiplying factor becomes larger and therefore the strain sensitivity increases. All this is confirmed by the results shown in Figure 5.12. The obtained mean strain sensitivity to the taper size determined was $(2.7 \pm 0.1) \times 10^{-2}\,\varepsilon^{-1}\,(\mu\mathrm{m}/\mu\mathrm{m})$. Sensitivities of $-1.73\,\mathrm{pm}/\mu\varepsilon$ for the $120\,\mu$m taper and $-3.12\,\mathrm{pm}/\mu\varepsilon$ for the $70\,\mu$m taper were obtained. An increase in strain sensitivity of approximately 80% was detected. Also plotted in Figure 5.12 is the theoretical estimate given by equation 2.9:

$$\kappa_{taper} = \kappa_0 \frac{L_{fiber} + L_{taper}}{L_{fiber}\frac{d_{taper}^2}{d_{fiber}^2} + L_{taper}}. \tag{5.4}$$

From this it is possible to estimate κ_0 to be $-1.7\,\mathrm{pm}/\mu\varepsilon$. This approximation is within experimental error, which confirms the applicability of the previous strain sensitivity approximation to these tapers.

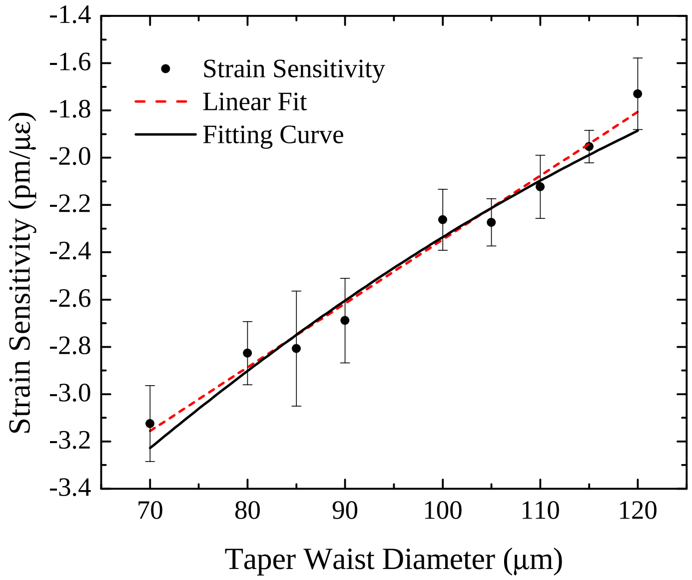

Figure 5.12 – Relationship between strain sensitivity and taper waist diameter. A linear fit and a theoretical fit to expression 5.4 are represented.

5.3.5 Temperature Characterization

Figure 5.13 presents the spectral response of the $70\,\mu$m SCF taper at 30 °C and 70 °C, where no discernible wavelength shift can be detected. This result is expected due to the properties of the SCF – the fiber is made of pure silica and its thermo-optic coefficient is very low.

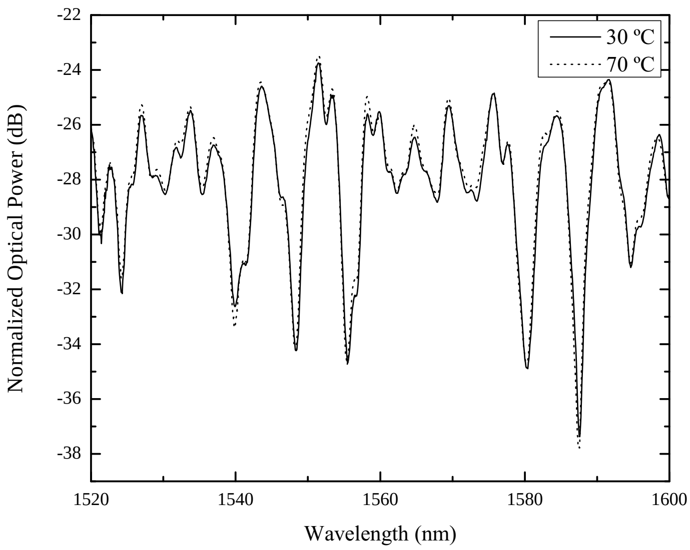

Figure 5.13 – Spectral response of the 70 μm taper at 30 °C and 70 °C.

5.3.6 Refractive Index Characterization

The tapers were immersed in ethanol but no change whatsoever was visible in the spectral response. This was due to the fact that the holes did not collapse even at high diameter reductions. This fact combined with the existence of big holes present inside the fiber, isolate the fiber core from the exterior index of refraction. Basically, since the guided modes are very well confined inside an air-silica waveguide (high index difference), the evanescent field outside of the fiber is basically null and therefore it is insensitive to the refractive index of the liquid in which the taper is immersed.

5.4 Discussion

Tapers from 40 μm (core $\phi \sim 2.4\,\mu$m) to 120 μm (core $\phi \sim 8\,\mu$m) in diameter were produced on an originally 125 μm diameter SCF. They were characterized in terms of strain, temperature, and external refractive index. They were deemed insensitive to temperature and external refractive index, but extremely sensitive to strain. Through the analysis of transverse sections it was possible to show that the holes did not collapse even at 40 μm cladding diameter. Sensitivities of up to $-3.12\,\mathrm{pm}/\mu\varepsilon$ for the 70 μm taper structure were obtained and consequently an increase of 80% in sensitivity was achieved. An increase of strain sensitivity with decreasing taper diameter was observed [67].

These tapered suspended core fiber structures have advantages when compared to normal fiber tapers as sensing elements. Besides displaying enhanced strain sensitivity, they also have very low temperature sensitivity and are protected from external medium perturbations due to the strong confinement of light in an air-silica waveguide.

One advantage evident from this study is the possibility to obtain different sensitivities with this type of sensor. A new sensing head for simultaneous measurement of different physical parameters (curvature and pressure, for example) can be designed. A possible solution is to use two tapers with different diameters spliced in series with an appropriate interrogation system. Another possibility is combining this sensor with other types of optical fiber sensors, such as Fiber Bragg Gratings (FBG) or Long Period Gratings (LPG).

Chapter 6

Micro/Nanotapers in Suspended Core Fiber

6.1 Introduction

6.1.1 Fiber Loop Mirror Configuration

Fiber loop mirrors (FLMs) are frequently used devices in optical communications and sensing [68]. This device has attracted a lot of attention because it is very easy to manufacture. It is formed by a splice between the output ports of an optical coupler. In this configuration, two waves travel inside the fiber loop in opposite directions but following the same optical paths, which assures constructive interference when the waves recombine at the coupler. This way, all the light is reflected back into the input port with reflectivity limited only by losses in the fiber, the splices, and the coupler. This mirror-like property is the reason why this device is frequently used to form a resonant cavity in fiber lasers [69].

This interferometric configuration is not a new concept but with the emergence of novel microstructured optical fibers, such as photonic crystal fibers (PCFs), it has again been subject of intense research. When introduced a section of high-birefringence fiber is introduced inside the fiber loop, obtaining a high-birefringence fiber loop mirror (HiBi-FLM), several advantages arise: independence of input polarization and the fact that the periodicity of the spectral filter produced is only dependent on the length of the HiBi fiber and not on the total length of the FLM [70].

HiBi-FLMs have been applied for dispersion compensation [71], gain flattening of Erbium-doped fiber amplifiers [72], multiwavelength fiber lasers [73], and tunable dual-wavelength fiber lasers [74], among others. In sensing, it has been used for strain [75], temperature [76, 77], and liquid-level measurement [78]. They have also been combined with LPGs [79] or FBGs [80] for simultaneous measurement of strain and temperature. More recently, a simple HiBi-FLM has been demonstrated as a multiparameter, strain and temperature sensor without the aid of any other structure [81].

6.1.2 Operation Method

In this subsection, a brief theoretical analysis of a HiBi-FLM with only one section HiBi fiber is performed [70]. The FLM can be modeled as shown in Figure 6.1. The incident light beam enters through port 1 and is split into two beams in the coupler. One beam will propagate clockwise while the other will propagate counterclockwise. Each of these beams will be decomposed into two others after they traverse a HiBi fiber section, correspondent to the slow and fast axis of the fiber. After completing the loop, the counterpropagating beams will recombine at the coupler and interfere according to the phase difference between them.

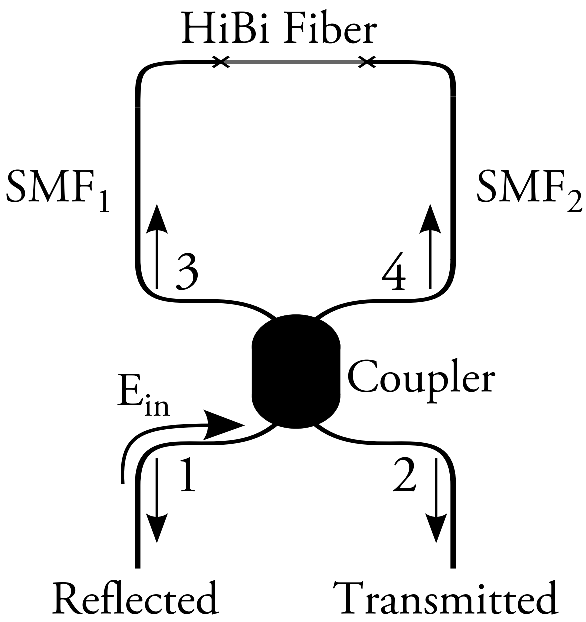

Figure 6.1 – Schematic of a fiber loop mirror.

At the input port 1 of the coupler, the input light field amplitudes are given by

$$E_{\text{in}} = \begin{bmatrix} E_x\text{in} \\ E_y\text{in} \end{bmatrix}, \tag{6.1}$$

and the output light at ports 3 and 4 is given by

$$E_3 = \sqrt{k}E_{\text{in}},\ E_4 = \sqrt{1-k}HE_{\text{in}}, \tag{6.2}$$

respectively, where k is the power-splitting ratio of the coupler, which will be taken to be 0.5 (3dB coupler), and H is the phase delay matrix introduced when light propagates through the cross arm of the coupler from port 1 to port 4. H is a simple phase retarding matrix whose general form is

$$T(\phi_x, \phi_y) = \begin{bmatrix} e^{i\phi_x} & 0 \\ 0 & e^{i\phi_y} \end{bmatrix}, \tag{6.3}$$

which for this particular case leads to

$$T(\pi/2, \pi/2) \equiv H = \begin{bmatrix} e^{i(\pi/2)} & 0 \\ 0 & e^{i(\pi/2)} \end{bmatrix}. \tag{6.4}$$

Considering the fiber loss and the SMF birefringence in the loop to be negligible, the transfer matrices of the clockwise and counterclockwise propagating beams when they propagate through a round trip and recombine at the coupler can be written as

$$\begin{aligned} M_{cw} &= R_2 T_1 R_1 \\ M_{ccw} &= R_1^{-1} T_1 R_2^{-1} \end{aligned} \tag{6.5}$$

where T_1 is the phase delay matrix that corresponds to the section of HiBi fiber, which can be deduced from the Jones matrix for a general phase retarder. As before, assuming the fast axis is aligned with the x or y directions:

$$\begin{aligned} T_1(\phi_{fast}, \phi_{slow}) = \begin{bmatrix} e^{i\phi_{fast}} & 0 \\ 0 & e^{i\phi_{slow}} \end{bmatrix} &= \begin{bmatrix} e^{-i\frac{2\pi l}{\lambda}n_{fast}} & 0 \\ 0 & e^{-i\frac{2\pi l}{\lambda}n_{slow}} \end{bmatrix} \\ &\downarrow \\ \phi_{fast,slow} &= \frac{2\pi l}{\lambda}n_{fast,slow} \end{aligned} \tag{6.6}$$

and R_j ($j = 1,\ 2$) is the rotation matrix that translates the rotation of the polarization state from port 3 to the HiBi fiber ($j = 1$) and from the HiBi fiber to port 4 ($j = 2$):

$$R_j = \begin{bmatrix} \cos(\theta_j) & -\sin(\theta_j) \\ \sin(\theta_j) & \cos(\theta_j) \end{bmatrix}, \quad j = 1, 2. \tag{6.7}$$

This angle θ_j is basically the angle between the polarization in the SMF and the fast axis of the HiBi fiber. For anticlockwise light, the rotation angle of the polarization state is $-\theta_j$, and thus the rotation matrix becomes $R_j^{-1} \left(= R_j^T\right)$.

After both clockwise and counterclockwise light beams complete the loop, they interfere at the coupler. The clockwise beam has to cross over to the coupler's other arm and therefore is affected by the factor $\sqrt{1-k}H$ while the counterclockwise beam does not and is affected by $\sqrt{k}$. The reflected light field's amplitude at port 1 can be written as

$$\begin{aligned} E_{1\text{out}} &= \underbrace{\sqrt{1-k}H}_{\text{cross arm}} M_{cw} E_3 + \sqrt{k} M_{ccw} E_4 \\ &= \sqrt{k(1-k)} \left[H R_2 T_1 R_1 + R_1^{-1} T_1 R_2^{-1} H \right] E_{\text{in}} \\ &= K_r E_{\text{in}}, \end{aligned} \tag{6.8}$$

where K_r is referred to as the reflected transfer matrix of the HiBi-FLM. The transmitted light field's amplitude at port 2 can then easily be written as

$$\begin{aligned} E_{2\text{out}} &= \sqrt{k} M_{cw} E_3 + \sqrt{1-k} H M_{ccw} E_4 \\ &= \left[k R_2 T_1 R_1 + (1-k) H R_1^{-1} T_1 R_2^{-1} H \right] E_{\text{in}} \\ &= K_t E_{\text{in}}, \end{aligned} \tag{6.9}$$

where K_t is the transmitted transfer matrix of the HiBi-FLM.

Calculating the reflected and transmitted intensities at ports 1 and 2 one obtains

$$I_{1\text{out}} = \left(E_{1\text{out}}^*\right)^T E_{1\text{out}} = \left(K_r^* E_{\text{in}}^*\right)^T K_r E_{\text{in}} \tag{6.10}$$

$$I_{2\text{out}} = \left(E_{2\text{out}}^*\right)^T E_{2\text{out}} = \left(K_t^* E_{\text{in}}^*\right)^T K_t E_{\text{in}}. \tag{6.11}$$

The reflectivity and transmittivity are given by

$$R = \frac{I_{1\text{out}}}{I_{\text{in}}} = \frac{\left(K_r^* E_{\text{in}}^*\right)^T K_r E_{\text{in}}}{E_{\text{in}}^* E_{\text{in}}} \tag{6.12}$$

$$T = \frac{I_{2\text{out}}}{I_{\text{in}}} = \frac{\left(K_t^* E_{\text{in}}^*\right)^T K_t E_{\text{in}}}{E_{\text{in}}^* E_{\text{in}}} \tag{6.13}$$

respectively. Substituting the values for the specific HiBi-FLM considered, explicit expressions for both R and T can be derived

$$R = 1 - \left[\sin\left(\theta\right)\cos\left(\phi/2\right)\right]^2 \tag{6.14}$$

$$T = \left[\sin\left(\theta\right)\cos\left(\phi/2\right)\right]^2 \tag{6.15}$$

where $\phi = 2\pi l B/\lambda$ (B is the phase modal birefringence and l the length of HiBi fiber) and $\theta = \theta_1 + \theta_2$. The cosine factor in equations 6.14 and 6.15 refers to the phase difference of the modal interferometer, while the sine factor is associated with the interferometer's visibility, being maximum for $\theta = \pi/2$. This angle θ can be controlled by applying a polarization controller to one of the SMF sections of the fiber loop mirror. This way, through rotation, the angle the polarization makes with the fast axis of the HiBi fiber can be controlled and the visibility is maximized.

When employing an optical fiber (as with any optical device), one should consider its birefringence to be dispersive. By definition, the phase modal birefringence is given by

$$B\left(\lambda\right) = n_x\left(\lambda\right) - n_y\left(\lambda\right) = \frac{\lambda}{2\pi}\left(\beta_x\left(\lambda\right) - \beta_y\left(\lambda\right)\right), \tag{6.16}$$

where β_x and β_y are the propagation constants associated with each of the polarizations of the fundamental mode, i.e. the fast and slow modes of the fiber. This birefringence is associated with the beat length (L_B) as follows:

$$L_B = \frac{\lambda}{B\left(\lambda\right)}. \tag{6.17}$$

The group modal birefringence ($G\left(\lambda\right)$) is given by:

$$\begin{aligned} G(\lambda) &= \frac{d\beta_x(\lambda)}{dk} - \frac{d\beta_y(\lambda)}{dk} = \frac{d}{dk}(B(\lambda)\cdot k) \\ &= B(\lambda) - \lambda\frac{dB(\lambda)}{d\lambda} \end{aligned} \tag{6.18}$$

where $k = 2\pi/\lambda$. The phase difference that results between the two polarization modes after propagation over a length L of fiber is

$$\phi = k\cdot OPD = \frac{2\pi}{\lambda}L\cdot(n_x - n_y) = \frac{2\pi L\cdot B(\lambda)}{\lambda}. \tag{6.19}$$

Differentiating the phase with respect to λ,

$$\frac{d\phi}{d\lambda} = \frac{2\pi L}{\lambda^2}\left[\lambda\frac{dB(\lambda)}{d\lambda} - B(\lambda)\right] = -\frac{2\pi L}{\lambda^2}G(\lambda). \tag{6.20}$$

If one defines $\Delta\lambda$ as the spatial period of the fringes present in the spectral response, which corresponds to a phase shift of 2π, an expression for the group modal birefringence can be deduced:

$$G(\lambda) = -\frac{\lambda^2}{\Delta\lambda\cdot L}. \tag{6.21}$$

6.2 Fabrication and Characterization

6.2.1 Suspended Core Fiber

The suspended core fiber used in this work was produced at the IPHT and its cross-section can be seen in Figure 6.2 along with its specifications. The suspended core fiber used has a narrow Ge-doped core inside the suspended core that will only elevate even more the index difference between core and cladding, as opposed to an all-silica suspended core. This Ge-core will likely have no influence whatsoever when tapering the fiber because it will most likely disappear. Due to the high temperatures, the Ge-core will diffuse through the suspended-core and present itself in a very low concentration. The sensing heads are composed of a section of approximately 50 mm of suspended core fiber spliced between standard singlemode fibers.

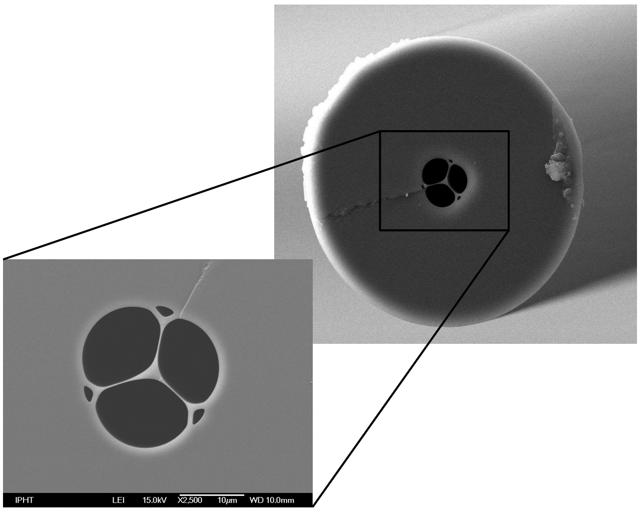

Specification	Sizes
$\varnothing_{\text{fiber}}$ (μm)	125.6
$\varnothing_{\text{core}}$ (μm)	2.1
$\varnothing_{\text{Ge core}}$ (μm)	0.7
d_{hole} (radial) (μm)	10.7
d_{hole} (azimuthal) (μm)	14.3
bridges (nm)	228.0 169.2 197.2

Figure 6.2 – Suspended core fiber micrograph and specifications.

6.2.2 Taper Fabrication

The VYTRAN GPX-3400 was used to produce the tapers. Its characteristics and operation were already discussed in Chapter 2. The taper dimensions aimed for were 15 mm for the up taper and down taper lengths, and 10 mm for the taper waist length. Sometimes, due to uncertainties intrinsic to the VYTRAN, these dimensions were a little off. If the dimensions were significantly different from the desired ones or the taper was too asymmetric, the sample would be discarded and a new one would be produced.

6.2.3 Strain and Temperature Characterization

Similar procedures to those explained in Section 5.2.3 were used to characterize the taper structures. For temperature, the fiber was placed inside a thermalized water bath and its temperature measured. For strain, the fiber was attached to micrometric translation stages and gradual stress was applied to it.

6.3 Results

6.3.1 Cross Section Analysis

By analyses of the cross-sections of several taper waists one can see that the core geometry is maintained as the diameter is reduced and no hole collapse occurs down to 20 μm of outer diameter. The relationship between core diameter and cladding diameter is represented in Figure 6.3a. A taper region with a sub-micron core can easily be produced using the VYTRAN-GPX. The hole structure does collapse when reducing the cladding diameter to 10 μm, as seen in Figure 6.3b.

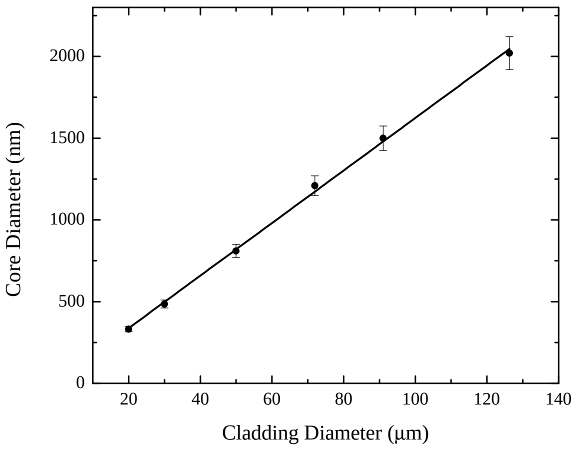

(a) Relationship between core and cladding.

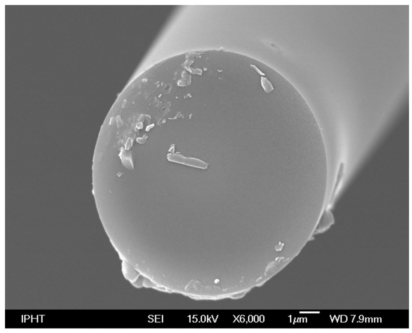

(b) Micrograph of a cleaved 10 μm-taper.

Figure 6.3 – Cross-section analysis of core and cladding.

6.3.2 Simulations

BPM was used to perform simulations providing the number of modes that propagate in the three-hole suspended core fiber. An approximate expression for the number of modes as a function of the normalized frequency was obtained and is as follows:

$$N \approx \frac{V^2}{3}. \tag{6.22}$$

Comparing this with the expression for the number of modes of a standard multimode fiber ($N = V^2/2$) and the four-hole SCF previously analyzed in Chapter 5 ($N \approx V^2/5$) one can see that the three-hole case lays somewhere in the middle. Figure 6.4 illustrates this well by plotting the number of modes against the core diameter.

It should be noted that these are the total number of modes that can propagate

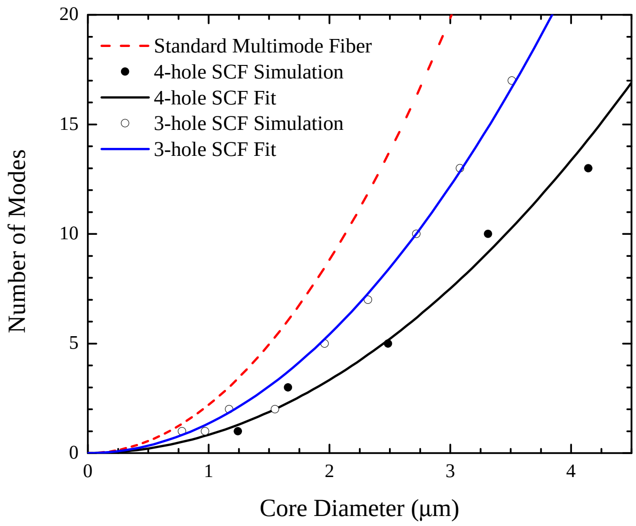

Figure 6.4 – Relationship between the number of modes and the core diameter of the suspended core three-hole and four-hole fiber. Also included are quadratic fits to both data sets.

inside the fiber. That does not mean that they all exist in our case because they may either not be excited, be lost in the taper transitions or simply not be relevant enough on such a short piece of fiber. By analyzing Figure 6.4, it is possible to estimate at which core diameter value only two modes propagate inside the fiber. The region below 1 μm seems to propagate only two modes. The two lowest order modes are shown in Figure 6.5. In principle, by reaching a diameter of 810 nm (50 μm-taper), only two modes should propagate through the taper.

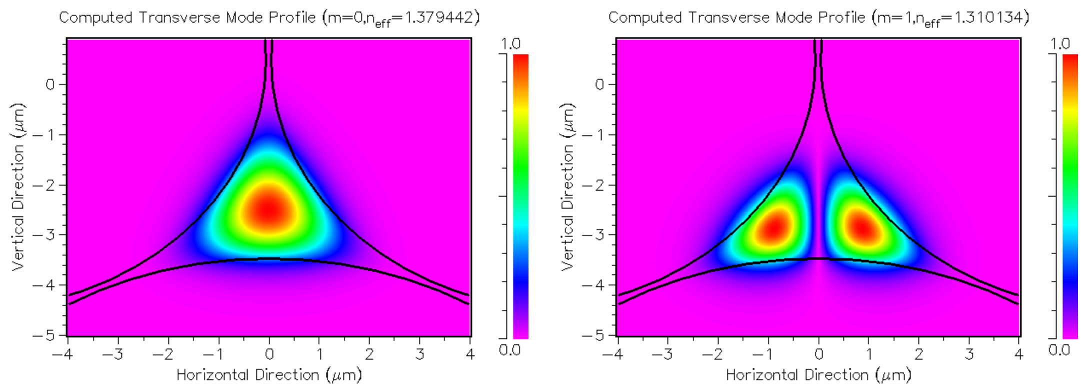

(a) Fundamental mode. **(b)** First higher order mode

Figure 6.5 – BPM simulations of the lowest order modes guided in the three-hole suspended core fiber used.

6.3.3 Spectral Response Analysis

Figure 6.6 illustrates the experimental setup used in this work. It consists of an optical broadband source, a fiber loop mirror (FLM), and an optical spectrum analyzer (OSA) with a maximum resolution of 0.01 nm. The optical source is an erbium-doped broadband source, with a central wavelength of 1550 nm and a spectral bandwidth of 100 nm. The FLM is formed by a 3dB (2×2) optical coupler with low insertion loss, a section of suspended core fiber with approximately 50 mm length, and an optical polarization controller.

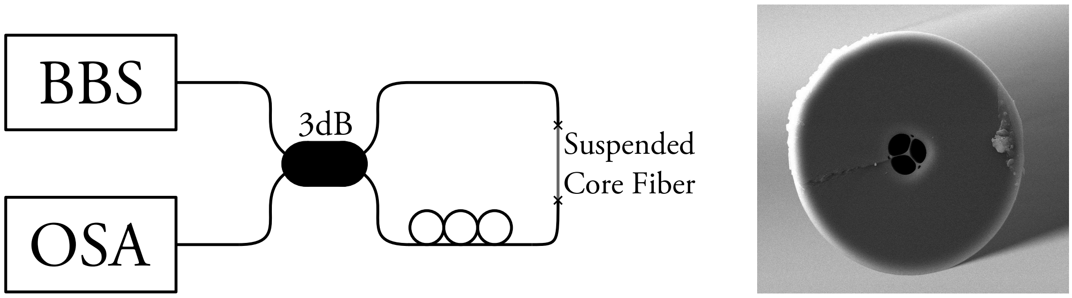

Figure 6.6 – Fiber Loop Mirror (FLM) configuration including a Broadband Source (BBS), an Optical Spectrum Analyzer (OSA), a 3dB coupler, a polarization controller and a section of Suspended Core Fiber (SCF).

Analyzing the spectral response of the FLM with a section of untapered fiber, one can easily observe two different interferometers: one that results from the fiber's high birefringence (large-period fringes – Figure 6.7b) and one that results from intermodal interference (short-period fringes – Figure 6.7a). Going to smaller taper waists, the intermodal interference becomes weaker and weaker and at a core diameter of 810 nm (50 μm cladding diameter) the group birefringence is completely dominant and the intermodal fringes are barely visible (see Figure 6.7). This is in accordance with the previous simulations, where at 50 μm of cladding diameter (810 nm of core diameter), only two modes seem to exist.

6.3.4 Group Birefringence Analysis

Using equation 6.21, it becomes easy to assess the group birefringence of the fiber or fiber structure, such as a tapered fiber, from a spectrum as seen in Figure 6.7b. Since the considered fiber has a triangular core, it is expected to have a high group birefringence. It in fact has a group birefringence of 3.04×10^{-3} in the 1550 nm-region. As the fiber is tapered down to a smaller taper waist, the group birefringence increases until it reaches a maximum (see Figure 6.8). It then decreases when further

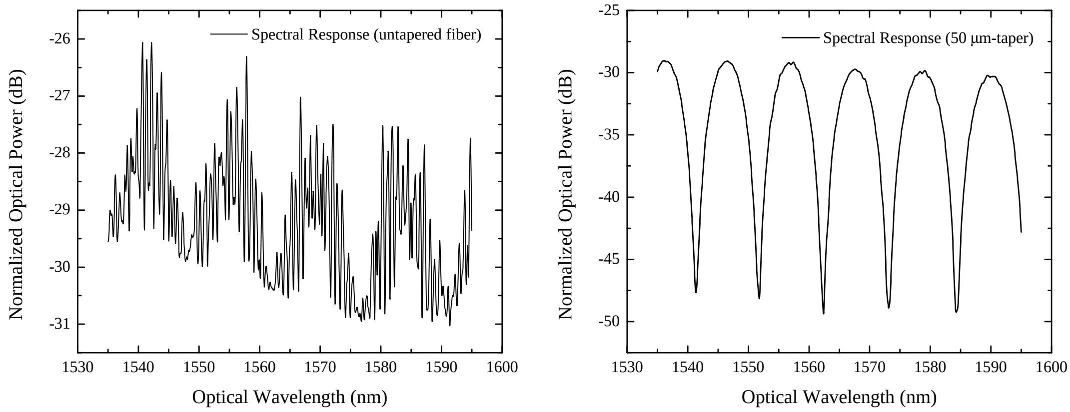

(a) Spectral response of the FLM containing a section of untapered suspended core fiber.

(b) Spectral response of the FLM containing a section of 50 μm-tapered suspended core fiber.

Figure 6.7 – Spectral responses of two different sensing heads.

decreasing the diameter. The increase is easily explained by the additional stresses introduced in the taper region. But that does not explain why the group birefringence decreases when taking the core diameter down to 810 nm. This is likely due to the fact that, since the wavelength of light is much larger than the core (1550 nm > 810 nm), the modal profile is so big compared to the core that it no longer depends on its geometrical shape.

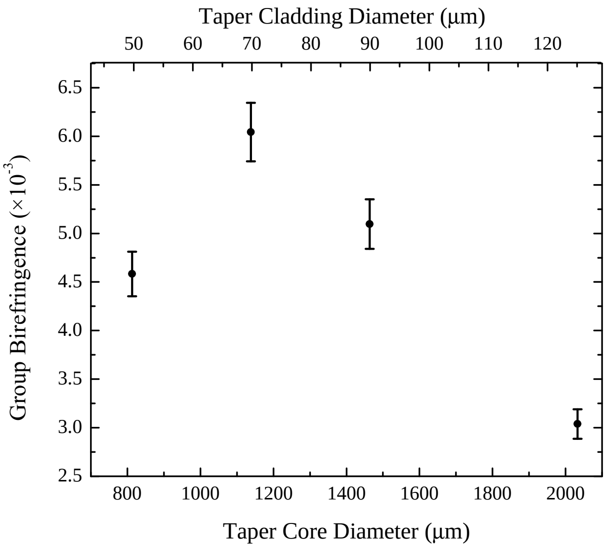

Figure 6.8 – Group birefringence variation with taper waist diameter in the 1550 nm region.

6.3.5 Strain Behavior of Suspended Nano-core Tapers

For strain characterization, each sensing head was placed on micrometric translation stages and subjected to controlled stretching. A total length of 0.5 m was subjected to strain. To determine the wavelength variations, the wavelength change of the main peaks was monitored through an optical spectrum analyzer with a maximum resolution of 0.01 nm (see Figure 6.9a). Figure 6.9b shows an increase in strain sensitivity as the taper waist diameter is decreased. A maximum strain sensitivity of $-2.41\,\mathrm{pm}/\mu\varepsilon$ was obtained for the 50 μm taper (810 nm core). This results in an increase of 236 % relative to the sensitivity of the untapered fiber ($-0.718\,\mathrm{pm}/\mu\varepsilon$).

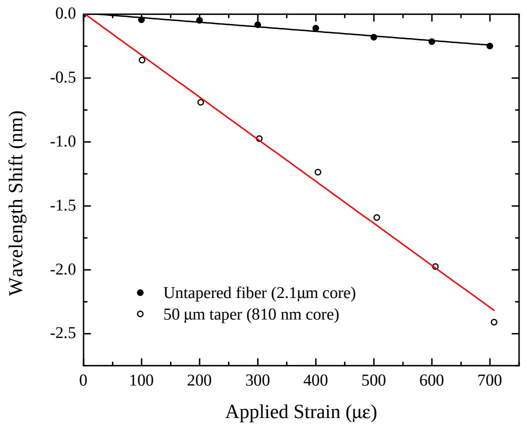

(a) Wavelength shift with applied strain for the untapered SCF ($\O_{core} = 2.1\,\mu$m) and the 50 μm taper ($\O_{core} = 810$ nm).

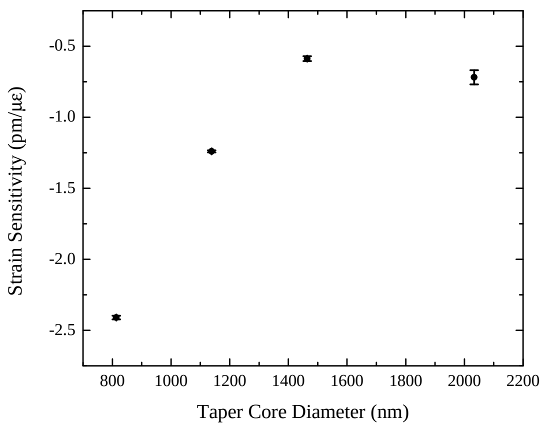

(b) Strain sensitivity as a function of the taper core's diameter.

Figure 6.9 – Strain analysis of the suspended nano-core tapers.

6.3.6 Temperature Analysis

The sensing heads were characterized with respect to temperature variations in the range 35 °C to 85 °C. In Figure 6.10 the wavelength shift of the group birefringence fringe pattern is analyzed as a function of the temperature variation for the untapered 125 μm suspended-core fiber and the 50 μm taper. For the untapered case, a very low sensitivity of $-2.1\,\mathrm{pm}/\mathrm{K}$ is determined, which is due to the germanium doped nano-core present inside the suspended core. But when considering the 50 μm-taper, which has a very small core of only 810 nm, a very high sensitivity of $-56.2\,\mathrm{pm}/\mathrm{K}$ is obtained. This is due to the high stresses present in the tapered sample since its fabrication. Since the taper is produced at a very high temperature and then quenched to ambient temperature very fast, high stresses are trapped in the taper structure.

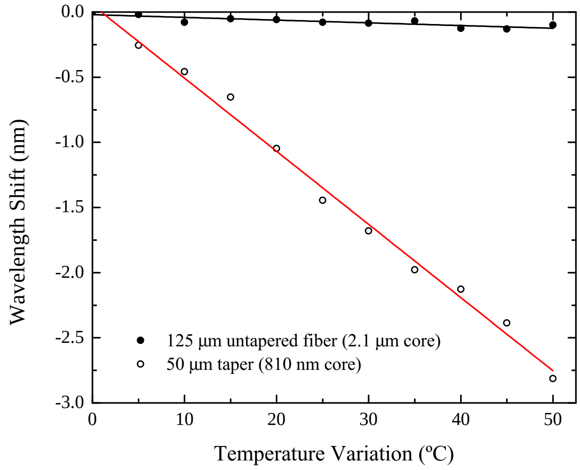

Figure 6.10 – Temperature sensitivities of the untapered fiber and the 50 μm taper (810 nm core).

6.4 Discussion

Tapers of several waist diameters were produced on three-hole suspended core fiber with an original core diameter of 2.1 μm. The fiber was tapered down to 20 μm without hole collapse, achieving a core diameter of 330 nm. Below an external diameter of 50 μm light could no longer be guided inside the nanometric core (810 nm) and cladding guidance took over. This was readily observed with a change in spectral response to a multimode interference pattern due to the existence of many modes. The tapers were then introduced in a fiber loop mirror for further characterization. The group birefringence was determined to increase as the diameter of core and cladding decrease until a point where it again decreases. A group birefringence of 6.0×10^{-3} was calculated for the 70 μm-taper (1.2 μm). As the core diameter is reduced, the number of guided modes is consequently reduced, and as seen both through the simulations and the spectral responses, the intermodal interference is reduced. At 810 nm, only two modes seem to propagate and the interference pattern reduces to a two-wave interferometer.

Strain sensitivity increases with taper waist reduction. A sensitivity of $-2.41\,{}^{\text{pm}}/_{\mu\varepsilon}$ was obtained for the 50 μm-taper (810 nm core), 3.4 times larger than the untapered fiber's sensitivity. As for temperature, a very high sensitivity of $-56.2\,{}^{\text{pm}}/_{K}$ for the same taper was obtained, as opposed to the low sensitivity of $-2.1\,{}^{\text{pm}}/_{K}$ for the untapered case. This is most likely due to stresses induced in the taper region when the taper is produced, that are then trapped once the structure returns to ambient temperature.

Chapter 7

Final Conclusions and Future Work

The focus of this dissertation is the study of microwire structures based on fiber tapers and the advantages of tapering instead of using untapered fiber structures. A configuration for simultaneous measurement of strain and temperature is proposed using tapered multimode interference devices and has, as far as the author knows, the best condition number achieved in literature. This allows for very accurate measurement and low associated errors. It was proved that tapering long period gratings greatly increases their sensitivity to strain. Suspended core fibers have been efficiently tapered down by a ratio of 6 without any change in cross section and any special measure to prevent hole collapse. Strain sensitivities have been enhanced by tapering in three different types of structures: multimode interference devices, long period gratings, and suspended core fibers. Two papers have been written of which one has been published and the other accepted. *Strain sensitivity enhancement in suspended core fiber tapers [67]* was published in Photonic Sensors journal and *Simultaneous strain and temperature measurement based on multimode interference in tapered fiber structures [48]* has been accepted by Photonics Technology Letters.

Some conclusions are drawn about how much does tapering the fiber actually enhance its sensitivity to physical parameters, specifically strain. Table 7.1 summarizes the maximum strain sensitivities obtained with each tapered structure. The highest strain sensitivity obtained was with the long period grating fabricated on a taper. Even though it has the highest sensitivity, this structure is one of the hardest to produce because producing the LPG on such a thin section of fiber easily leads to it breaking. The most adequate structure for strain sensing, of the ones analyzed, is the tapered MMI. Not only is the strain sensitivity very high but it is fairly easy to fabricate.

As for the suspended core fibers, the strain sensitivities obtained are not very

Strain Sensitivities ($\mathrm{pm}/\mu\varepsilon$)		
	Maximum Sensitivity	Untapered Sensitivity
Tapered MMI	-23.69	-2.08
Tapered LPG	-24.8	-0.90
4-hole SCF ($4.8\,\mu$m – core)	-3.12	-1.74
3-hole SCF (810 nm – core)	-2.41	-0.72

Table 7.1 – Comparison of strain sensitivities for the several structures studied.

high. For the 4-hole case, the taper diameter is not very low ($70\,\mu$m) corresponding to a core diameter of $4.4\,\mu$m. This means that by decreasing the waist diameter, it would be possible to further increase the sensitivity. Since the core size is still much larger than the wavelength of light used ($1.550\,\mu$m) no major loss problems should arise when tapering to lower diameters. As for the 3-hole case, the taper diameter is as low as can be without completely changing the propagating conditions and thus the spectral response of the sensor. The sensing head was introduced in a fiber loop mirror due to its intrinsic geometric birefringence and a higher sensitivity was expected, but that was not the case.

As for temperature sensitivity, only the tapers in MMIs and SCFs were characterized, and of these only the tapered MMIs and the three-hole SCF were deemed sensitive. With the MMIs, the lower the taper diameter, the lower the temperature sensitivity is ($16.56\,\mathrm{pm}/\mathrm{K}$). The opposite occurs with the three-hole SCF tapers. A very small sensitivity is obtained for the untapered SCF ($-2.1\,\mathrm{pm}/\mathrm{K}$) and a very large one for the $50\,\mu$m-taper ($-56.2\,\mathrm{pm}/\mathrm{K}$). This difference indicates that different processes are at work. In the MMI case the reduction is due to a smaller volume of material being susceptible of thermal expansion. In the SCF case, the increase in sensitivity is due to the introduction of stresses during fabrication that are higher the lower the diameter is. Another relevant fact is that while the sensitivities for the tapered MMI are of the same order of magnitude, for the SCF the difference is more than one order of magnitude. It is suspected that the reason why the three-hole SCF is sensitive to temperature as opposed to the four-hole SCF is because of the presence of a small germanium core in the three-hole fiber.

For simultaneous measurement of strain and temperature, only the tapered MMIs were considered due to the cross-sensitivity between strain and temperature. When considering two sensors, the one with the highest strain sensitivity must have the lowest temperature sensitivity in order to have a very stable system. Because of this, a system with two tapered MMIs with different diameters is ideal for simultaneous measurement of strain and temperature, and a very low matrix condition number confirms the fact.

For the future, several extensions of the work presented in this thesis are planned:

- As a continuation of the tapers in MMI devices, multiplexing of the sensors by arranging them in a parallel configuration may lead to a useful setup for multiparameter sensing;
- The combination of two LPGs, one tapered and one not, initially with loss peaks at different wavelengths, may be used for high sensitivity strain sensing through a Mach Zehnder interferometric configuration;
- To further explore the tapering of suspended core fiber, a continuation of the tapering of the four-hole suspended core fiber to lower taper diameters may be relevant. By going to lower taper waist diameters, a deeper understanding of what is really going on in terms of mode interaction will result from such study;
- Tapering other types of microstructured fibers, such as a suspended twin-core fiber may be interesting in order to achieve coupling between the two cores.

References

[1] J. C. Knight, T. A. Birks, P. S. J. Russell, and D. M. Atkin. All-silica single-mode optical fiber with photonic crystal cladding. *Optics Letters*, 21(19):1547–1549, 1996.

[2] J. K. Ranka, R. S. Windeler, and A. J. Stentz. Visible continuum generation in air-silica microstructure optical fibers with anomalous dispersion at 800 nm. *Opt. Lett.*, 25(1):25–27, Jan 2000.

[3] S. J. Mihailov, C. W. Smelser, P. Lu, R. B. Walker, D. Grobnic, H. Ding, G. Henderson, and J. Unruh. Fiber bragg gratings made with a phase mask and 800-nm femtosecond radiation. *Opt. Lett.*, 28(12):995–997, Jun 2003.

[4] Y.-P. Wang, L. Xiao, D. N. Wang, and W. Jin. Highly sensitive long-period fiber-grating strain sensor with low temperature sensitivity. *Opt. Lett.*, 31(23):3414–3416, Dec 2006.

[5] R. Kenny, T. Birks, and K. Oakley. Control of optical fibre taper shape. *Electronics Letters*, 27(18):1654 –1656, aug. 1991.

[6] T. E. Dimmick, G. Kakarantzas, T. A. Birks, and P. S. Russell. Carbon dioxide laser fabrication of fused-fiber couplers and tapers. *Applied Optics*, 38(33):6845–6848, 1999.

[7] Z. Tian, S.-H. Yam, J. Barnes, W. Bock, P. Greig, J. Fraser, H.-P. Loock, and R. Oleschuk. Refractive index sensing with mach-zehnder interferometer based on concatenating two single-mode fiber tapers. *Photonics Technology Letters, IEEE*, 20(8):626 –628, april15, 2008.

[8] G. Brambilla, E. Koizumi, X. Feng, and D. J. Richardson. Compound-glass optical nanowires. *Electronics Letters*, 41(7):400–402, 2005.

[9] O. Frazão, R. Falate, J. L. Fabris, J. L. Santos, L. A. Ferreira, and F. M. Araújo. Optical inclinometer based on a single long-period fiber grating combined with a fused taper. *Optics Letters*, 31(20):2960–2962, Oct 2006.

[10] Z. Tian, S. S.-H. Yam, and H.-P. Loock. Refractive index sensor based on an abrupt taper michelson interferometer in a single-mode fiber. *Opt. Lett.*, 33(10):1105–1107, May 2008.

[11] B. S. Kawasaki, K. O. Hill, and R. G. Lamont. Biconical-taper single-mode fiber coupler. *Opt. Lett.*, 6(7):327–328, Jul 1981.

[12] K. Jedrzejewski, F. Martinez, J. Minelly, C. Hussey, and F. Payne. Tapered-beam expander for single-mode optical-fibre gap devices. *Electronics Letters*, 22(2):105 –106, 16 1986.

[13] T. Brophy, L. Bobb, and P. Shankar. In-line singlemode fibre interferometer via concatenated biconical tapers. *Electronics Letters*, 29(14):1276 –1277, july 1993.

[14] A. Kumar, T. Subrahmanyam, A. Sharma, K. Thyagarajan, B. Pal, and I. Goyal. Novel refractometer using a tapered optical fibre. *Electronics Letters*, 20(13):534 –535, 21 1984.

[15] L. Bobb, P. Shankar, and H. Krumboltz. Bending effects in biconically tapered single-mode fibers. *Lightwave Technology, Journal of*, 8(7):1084 –1090, jul 1990.

[16] L. C. Bobb, H. D. Krumboltz, and P. M. Shankar. Pressure sensor that uses bent biconically tapered single-mode fibers. *Opt. Lett.*, 16(2):112–114, Jan 1991.

[17] O. Frazao, M. Melo, P. V. S. Marques, and J. L. Santos. Chirped bragg grating fabricated in fused fibre taper for strain and temperature discrimination. *Measurement Science and Technology*, 16(4):984, 2005.

[18] Z. Tian and S.-H. Yam. In-line abrupt taper optical fiber mach-zehnder interferometric strain sensor. *Photonics Technology Letters, IEEE*, 21(3):161 –163, feb.1, 2009.

[19] O. Frazão, P. Caldas, F. M. Araújo, L. A. Ferreira, and J. L. Santos. Optical flowmeter using a modal interferometer based on a single nonadiabatic fiber taper. *Opt. Lett.*, 32(14):1974–1976, Jul 2007.

[20] Y. Lizé, E. Mägi, V. Ta'eed, J. Bolger, P. Steinvurzel, and B. Eggleton. Microstructured optical fiber photonic wires with subwavelength core diameter. *Optics Express*, 12(14):3209–3217, 2004.

[21] A. Hartung, A. M. Heidt, and H. Bartelt. Pulse-preserving broadband visible supercontinuum generation in all-normal dispersion tapered suspended-core optical fibers. *Optics Express*, 19(13):12275–12283, 2011.

[22] J. Villatoro, V. P. Minkovich, and D. Monzón-Hernández. Temperature-independent strain sensor made from tapered holey optical fiber. *Optics Letters*, 31(3):305–307, Feb 2006.

[23] T. A. Birks and Y. W. Li. The shape of fiber tapers. *Journal of Lightwave Technology*, 10(4):432–438, 1992.

[24] J. Love and W. Henry. Quantifying loss minimisation in single-mode fibre tapers. *Electronics Letters*, 22(17):912 –914, 14 1986.

[25] J. D. Love. Spot size, adiabaticity and diffraction in tapered fibers. *Electronics Letters*, 23(19):993–994, 1987.

[26] J. D. Love, W. M. Henry, W. J. Stewart, R. J. Black, S. Lacroix, and F. Gonthier. Tapered single-mode fibers and devices .1. adiabaticity criteria. *Ieee Proceedings-J Optoelectronics*, 138(5):343–354, 1991.

[27] R. Black, S. Lacroix, F. Gonthier, and J. Love. Tapered single-mode fibres and devices. ii. experimental and theoretical quantification. *Optoelectronics, IEE Proceedings J*, 138(5):355 –364, oct 1991.

[28] S. James, M. Dockney, and R. Tatam. Simultaneous independent temperature and strain measurement using in-fibre bragg grating sensors. *Electronics Letters*, 32(12):1133 –1134, jun 1996.

[29] L. Xiaohong, W. Dexiang, Z. Fujun, and D. Enguang. Simultaneous independent temperature and strain measurement using one fiber bragg grating based on the etching technique. *Microwave and Optical Technology Letters*, 43(6):478–481, 2004.

[30] O. Frazao, L. Marques, J. Marques, J. Baptista, and J. Santos. Simple sensing head geometry using fibre bragg gratings for strain and temperature discrimination. *Optics Communications*, 279(1):68 – 71, 2007.

[31] O. Frazão, S. F. O. Silva, A. Guerreiro, J. L. Santos, L. A. Ferreira, and F. M. Araújo. Strain sensitivity control of fiber bragg grating structures with fused tapers. *Applied Optics*, 46(36):8578–8582, 2007.

[32] L. Soldano and E. Pennings. Optical multi-mode interference devices based on self-imaging: principles and applications. *Journal of Lightwave Technology*, 13(4):615 –627, April 1995.

[33] A. Kumar, R. K. Varshney, S. A. C, and P. Sharma. Transmission characteristics of sms fiber optic sensor structures. *Optics Communications*, 219:215 – 219, 2003.

[34] Q. Wang, G. Farrell, and W. Yan. Investigation on single-mode–multimode–single-mode fiber structure. *Journal of Lightwave Technology*, 26(5):512–519, Mar 2008.

[35] A. Mehta, W. Mohammed, and E. Johnson. Multimode interference-based fiber-optic displacement sensor. *Photonics Technology Letters, IEEE*, 15(8):1129 – 1131, aug. 2003.

[36] W. Mohammed, A. Mehta, and E. Johnson. Wavelength tunable fiber lens based on multimode interference. *Journal of Lightwave Technology*, 22(2):469 – 477, feb. 2004.

[37] O. Frazão, S. O. Silva, J. Viegas, L. A. Ferreira, F. M. Araújo, and J. L. Santos. Optical fiber refractometry based on multimode interference. *Applied Optics*, 50(25):E184–E188, Sep 2011.

[38] W. S. Mohammed, P. W. E. Smith, and X. Gu. All-fiber multimode interference bandpass filter. *Optics Letters*, 31(17):2547–2549, Sep 2006.

[39] Q. Wang and G. Farrell. Multimode-fiber-based edge filter for optical wavelength measurement application and its design. *Microwave and Optical Technology Letters*, 48(5):900–902, 2006.

[40] P. Wang, G. Brambilla, M. Ding, Y. Semenova, Q. Wu, and G. Farrell. High-sensitivity, evanescent field refractometric sensor based on a tapered, multimode fiber interference. *Optics Letters*, 36(12):2233–2235, Jun 2011.

[41] W. Jin, W. C. Michie, G. Thursby, M. Konstantaki, and B. Culshaw. Simultaneous measurement of strain and temperature: error analysis. *Optical Engineering*, 36:598–609, February 1997.

[42] M. Davis and A. Kersey. Simultaneous measurement of temperature and strain using fibre bragg gratings and brillouin scattering. *Optoelectronics, IEE Proceedings -*, 144(3):151 –155, jun 1997.

[43] X. Shu, Y. Liu, D. Zhao, B. Gwandu, F. Floreani, L. Zhang, and I. Bennion. Dependence of temperature and strain coefficients on fiber grating type and its application to simultaneous temperature and strain measurement. *Opt. Lett.*, 27(9):701–703, May 2002.

[44] D.-P. Zhou, L. Wei, W.-K. Liu, Y. Liu, and J. W. Y. Lit. Simultaneous measurement for strain and temperature using fiber bragg gratings and multimode fibers. *Appl. Opt.*, 47(10):1668–1672, Apr 2008.

[45] E. Chehura, S. W. James, and R. P. Tatam. Temperature and strain discrimination using a single tilted fibre bragg grating. *Optics Communications*, 275(2):344 – 347, 2007.

[46] O. Frazao, L. Amaral, J. Baptista, P. Roy, R. Jamier, and S. Fevrier. Strain and temperature discrimination using modal interferometry in bragg fibers. *Photonics Technology Letters, IEEE*, 22(21):1616 –1618, nov.1, 2010.

[47] O. Frazao, J. P. Carvalho, L. A. Ferreira, F. M. Araujo, and J. L. Santos. Discrimination of strain and temperature using bragg gratings in microstructured and standard optical fibres. *Measurement Science and Technology*, 16(10):2109, 2005.

[48] R. M. Andre, C. R. Biazoli, M. B. Marques, C. M. B. Cordeiro, and O. Frazao. Simultaneous strain and temperature measurement based on multimode interference in tapered fiber structures. *Photonic Technology Letters*, pages DOI: 10.1007/s13320–012–0059–2, 2012.

[49] A. M. Vengsarkar, J. R. Pedrazzani, J. B. Judkins, P. J. Lemaire, N. S. Bergano, and C. R. Davidson. Long-period fiber-grating-based gain equalizers. *Optics Letters*, 21(5):336–338, Mar 1996.

[50] V. Bhatia. Applications of long-period gratings to single andmulti-parameter sensing. *Opt. Express*, 4(11):457–466, May 1999.

[51] V. Bhatia and A. M. Vengsarkar. Optical fiber long-period grating sensors. *Optics Letters*, 21(9):692–694, May 1996.

[52] S. A. Vasiliev and O. I. Medvedkov. Long-period refractive index fiber gratings: properties, applications, and fabrication techniques. In E. M. Dianov, editor, *Proc. SPIE, Moscow, Russia*, volume 4083, pages 212–223. SPIE, 2000.

[53] H. Patrick, G. Williams, A. Kersey, J. Pedrazzani, and A. Vengsarkar. Hybrid fiber bragg grating/long period fiber grating sensor for strain/temperature discrimination. *Photonics Technology Letters, IEEE*, 8(9):1223 –1225, sept. 1996.

[54] B. H. Lee and J. Nishii. Bending sensitivity of in-series long-period fiber gratings. *Opt. Lett.*, 23(20):1624–1626, Oct 1998.

[55] J.-F. Ding, A. Zhang, L.-Y. Shao, J.-H. Yan, and S. He. Fiber-taper seeded long-period grating pair as a highly sensitive refractive-index sensor. *Photonics Technology Letters, IEEE*, 17(6):1247 –1249, june 2005.

[56] T. Allsop, F. Floreani, K. P. Jedrzejewski, P. V. S. Marques, R. Romero, D. J. Webb, and I. Bennion. Spectral characteristics of tapered lpg device as a sensing element for refractive index and temperature. *Journal of Lightwave Technology*, 24(2):870, Feb 2006.

[57] W. Bock, J. Chen, P. Mikulic, and T. Eftimov. A novel fiber-optic tapered long-period grating sensor for pressure monitoring. *Instrumentation and Measurement, IEEE Transactions on*, 56(4):1176 –1180, aug. 2007.

[58] W. J. Bock, J. Chen, P. Mikulic, T. Eftimov, and M. Korwin-Pawlowski. Pressure sensing using periodically tapered long-period gratings written in photonic crystal fibres. *Measurement Science and Technology*, 18(10):3098, 2007.

[59] T. M. Monro, W. Belardi, K. Furusawa, J. C. Baggett, N. G. R. Broderick, and D. J. Richardson. Sensing with microstructured optical fibres. *Measurement Science and Technology*, 12(7):854, 2001.

[60] A. S. Webb, F. Poletti, D. J. Richardson, and J. K. Sahu. Suspended-core holey fiber for evanescent-field sensing. *Optical Engineering*, 46(1):010503–3, 2007.

[61] M. Rozé, B. Ung, A. Mazhorova, M. Walther, and M. Skorobogatiy. Suspended core subwavelength fibers: towards practical designs for low-loss terahertz guidance. *Optics Express*, 19(10):9127–9138, 2011.

[62] J. K. Chandalia, B. J. Eggleton, R. S. Windeler, S. G. Kosinski, X. Liu, and C. Xu. Adiabatic coupling in tapered air-silica microstructured optical fiber. *Ieee Photonics Technology Letters*, 13(1):52–54, 2001.

[63] S. T. Huntington, J. Katsifolis, B. C. Gibson, J. Canning, K. Lyytikainen, J. Zagari, L. W. Cahill, and J. D. Love. Retaining and characterising nano-structure within tapered air-silica structured optical fibers. *Optics Express*, 11(2):98–104, 2003.

[64] E. C. Magi, P. Steinvurzel, and B. J. Eggleton. Tapered photonic crystal fibers. *Optics Express*, 12(5):776–784, 2004.

[65] B. Y. Kim, J. N. Blake, S. Y. Huang, and H. J. Shaw. Use of highly elliptical core fibers for two-mode fiber devices. *Optics Letters*, 12(9):729–731, Sep 1987.

[66] K. Okamoto. *Fundamentals of optical waveguides*. Elsevier, 2006.

[67] R. M. André, S. O. Silva, M. Becker, K. Schuster, M. Rothardt, H. Bartelt, M. B. Marques, and O. Frazão. Strain sensitivity enhancement in suspended core fiber tapers. *Photonic Sensors*, 10.1007/s13320-012-0059-2, 2012.

[68] D. Mortimore. Fiber loop reflectors. *Lightwave Technology, Journal of*, 6(7):1217 –1224, jul 1988.

[69] P. Urquhart. Fiber lasers with loop reflectors. *Appl. Opt.*, 28(17):3759–3767, Sep 1989.

[70] Y. Liu, B. Liu, X. Feng, W. Zhang, G. Zhou, S. Yuan, G. Kai, and X. Dong. High-birefringence fiber loop mirrors and their applications as sensors. *Appl. Opt.*, 44(12):2382–2390, Apr 2005.

[71] S. Chung, B.-A. Yu, and B. Lee. Phase response design of a polarization-maintaining fiber loop mirror for dispersion compensation. *Photonics Technology Letters, IEEE*, 15(5):715 –717, may 2003.

[72] S. Li, K. Chiang, and W. Gambling. Gain flattening of an erbium-doped fiber amplifier using a high-birefringence fiber loop mirror. *Photonics Technology Letters, IEEE*, 13(9):942 –944, sept. 2001.

[73] X. Dong, S. Li, K. Chiang, M. Ng, and B. Chu. Multiwavelength erbium-doped fibre laser based on a high-birefringence fibre loop mirror. *Electronics Letters*, 36(19):1609 –1610, sep 2000.

[74] H. Sun, X. Liu, Y. Gong, X. Li, and L. Wang. Broadly tunable dual-wavelength erbium-doped ring fiber laser based on a high-birefringence fiber loop mirror. *Laser Physics*, 20:522–527, 2010. 10.1134/S1054660X10030175.

[75] M. Campbell, G. Zheng, A. S. Holmes-Smith, and P. A. Wallace. A frequency-modulated continuous wave birefringent fibre-optic strain sensor based on a sagnac ring configuration. *Measurement Science and Technology*, 10(3):218, 1999.

[76] E. D. la Rosa, L. A. Zenteno, A. N. Starodumov, and D. Monzon. All-fiber absolute temperature sensor using an unbalanced high-birefringence sagnac loop. *Opt. Lett.*, 22(7):481–483, Apr 1997.

[77] W. Qian, C.-L. Zhao, S. He, X. Dong, S. Zhang, Z. Zhang, S. Jin, J. Guo, and H. Wei. High-sensitivity temperature sensor based on an alcohol-filled photonic crystal fiber loop mirror. *Opt. Lett.*, 36(9):1548–1550, May 2011.

[78] D. Bo, Z. Qida, L. Feng, G. Tuan, X. Lifang, L. Shuhong, and G. Hong. Liquid-level sensor with a high-birefringence-fiber loop mirror. *Appl. Opt.*, 45(30):7767–7771, Oct 2006.

[79] O. Frazao, L. Marques, S. Santos, J. Baptista, and J. Santos. Simultaneous measurement for strain and temperature based on a long-period grating combined with a high-birefringence fiber loop mirror. *Photonics Technology Letters, IEEE*, 18(22):2407 –2409, nov.15, 2006.

[80] D.-P. Zhou, L. Wei, W.-K. Liu, and J. W. Lit. Simultaneous measurement of strain and temperature based on a fiber bragg grating combined with a high-birefringence fiber loop mirror. *Optics Communications*, 281(18):4640 – 4643, 2008.

[81] R. M. André, M. B. Marques, P. Roy, and O. Frazão. Fiber Loop Mirror Using a Small Core Microstructured Fiber for Strain and Temperature Discrimination. *IEEE Photonics Technology Letters*, 22(15):1120–1122, 2010.